Chemical gradients in automotive Cu-SSZ-13 catalysts for NO$_x$ removal revealed by operando X-ray spectrotomography

Johannes Becher[1], Dario Ferreira Sanchez[2], Dmitry E. Doronkin[1,3], Deniz Zengel[1], Debora Motta Meira[4,†], Sakura Pascarelli[4,‡], Jan-Dierk Grunwaldt[1,3,*], Thomas L. Sheppard[1,3,*]

[1] Institute for Chemical Technology and Polymer Chemistry (ITCP), Karlsruhe Institute of Technology (KIT), Engesserstr. 20, 76131 Karlsruhe, Germany

[2] Paul Scherrer Institut (PSI), 5232 Villigen, Switzerland

[3] Institute of Catalysis Research and Technology (IKFT), Karlsruhe Institute of Technology (KIT), Hermann-von-Helmholtz Platz 1, 76344 Eggenstein-Leopoldshafen, Germany

[4] European Synchrotron Radiation Facility (ESRF), 71 Avenue des Martyrs, 38000 Grenoble, France

†Current affiliation(s): CLS@APS Sector 20, Advanced Photon Source, Argonne National Laboratory, 9700 S. Cass Avenue, Argonne, IL 60439, USA; Canadian Light Source Inc., 44 Innovation Boulevard, Saskatoon, Saskatchewan S7N 2V3, Canada

‡Current affiliation: European XFEL GmbH, Holzkoppel 4, 22869 Schenefeld, Germany

Corresponding Authors: thomas.sheppard@kit.edu, grunwaldt@kit.edu

Abstract

NO_x emissions are a major source of pollution, demanding ever improving performance from catalytic aftertreatment systems. However, catalyst development is often hindered by limited understanding of the catalyst at work, exacerbated by widespread use of model rather than technical catalysts, and global rather than spatially-resolved characterisation tools. Here we combine operando X-ray absorption spectroscopy with microtomography to perform 3D chemical imaging of the chemical state of copper species in a Cu-SSZ-13 washcoated monolith catalyst during NO_x reduction. Gradients in copper oxidation state and coordination environment, resulting from an interplay of NO_x reduction with adsorption-desorption of NH_3 and mass transport phenomena, were revealed with micrometre spatial resolution while simultaneously determining catalytic performance. Crucially, direct 3D visualisation of complex reactions on non-model catalysts is only feasible using operando X-ray spectrotomography, which can improve our understanding of structure-activity relationships including the observation of mass and heat transport effects.

Due to health and environmental concerns, there is currently a strong societal demand for improved air quality, driving strict emission limits for CO, NO_x, unburnt hydrocarbons and particulates. The primary means of mitigating such pollutants is through more efficient catalytic converters. Highly effective Cu-zeolite catalysts such as Cu-SSZ-13 (chabazite) are among the prominent recent examples of active materials for selective catalytic reduction of NO_x with ammonia (NH_3-SCR)[1,2].

2

Numerous theoretical and experimental studies have aimed to understand the mechanism of NH_3-SCR on Cu-chabazites on the molecular scale[3-8]. Notably, X-ray absorption spectroscopy (XAS) and infrared (IR) spectroscopy have been particularly successful in probing the structure and coordination of potentially active metal species as well as adsorbates and surface chemistry, respectively. However, NH_3-SCR is a complex process involving variable Cu speciation and temperature-dependent reaction paths[9], further influenced by the NH_3 adsorption equilibrium[10], including NH_3 inhibition at low temperature[11-14]. In particular there is currently no consensus on the nature of the active site at elevated temperatures, since this also depends on position and local concentration of NH_3, NO and NO_2 in the catalyst bed. For example, both Cu(I) and Cu(II) species have been reported in literature at elevated temperature predominantly[1,3,8,9,13,14]. To shed light on the catalyst structure, it is thus necessary to perform in situ, preferably operando studies, under realistic reaction conditions (atmosphere, granulated catalyst) and coupled with catalytic performance measurements. However, despite being very demanding, spatiotemporal effects also need to be considered in case of temperature or concentration gradients[15-18]. This is because modern emission control systems, such as porous catalyst washcoats on monolith carriers, are rather structurally complex. Although studies based on plug flow reactors with granulated catalysts[14,16,18] or self-supported wafers[3,4] may facilitate data interpretation, such samples can be considered as non-realistic compared to typical technical catalysts, e.g. washcoated monoliths. In terms of the catalyst form, this oversimplification risks hiding the presence of local structural effects, which is particularly relevant when using global analytical methods such as XAS. In cases like NH_3-SCR, the catalytic converter optimally needs to be considered while at work, in a spatially-resolved manner, and on the molecular, meso- and macroscale.

In practice, in situ or operando characterisation of non-model catalysts is challenging. While molecular modelling combined with multi-scale simulations can virtually predict reaction steps, surface coverage, and concentration of reactants and products in specific volumes of a technical catalyst for example, ideally experimental data is required to validate such models[19,20]. Deviations in measured and predicted activity may indicate mass transport limitations, e.g. a slow effective diffusion of reactant and/or product gases in the solid catalyst[21], which can manifest as gradients within the catalyst particles. Although relatively simple to diagnose, such effects can be difficult to precisely characterise and especially difficult to control solely by optimising the catalyst design or simulating reaction behaviour[22]. To tackle this challenge of spatially-resolved characterisation, an ideal toolkit has emerged in the form of hard X-ray computed tomography (CT) performed at synchrotron light sources. The basis of X-ray CT is to non-invasively image the interior sample structure, allowing detection and co-localisation of sample constituents often with micro- or nanometre scale 3D spatial resolution[23]. X-ray CT can be coupled with various contrasts such as X-ray absorption, fluorescence, or diffraction, producing highly spatially-resolved chemical data which is unobtainable by contemporary methods[24-28]. This has been elegantly demonstrated for example for exhaust gas monoliths[29,30], fluid catalytic cracking particles[25,31], and Ziegler-Natta catalysts[32]. However, performing operando X-ray CT remains a significant challenge, requiring at least micrometre scale mechanical precision in 3D, free rotation of the reactor and unhindered X-ray transmission around 180°, maintaining reaction conditions, and ideally measuring catalytic activity at the same time. Several cutting-edge studies on powder or pelletised catalysts at work (i.e. model systems) have been published on Fischer-Tropsch synthesis[33-35], oxidative coupling of methane[36,37], and partial methane oxidation[38]. However, complex hierarchically-structured systems such as exhaust gas catalysts have not been investigated. In

4

particular quantitative catalytic activity data, which is crucial for accurate assessment of structure-activity relationships, has not yet been reported. Notably, the location and speciation of Cu in Cu-SSZ-13 catalysts has previously been explored with nanometre resolution by an alternative 3D imaging method known as atom probe tomography[39,40]. However, this method is completely destructive and operates in high vacuum, therefore it cannot be exploited for operando studies. Complementary sample-preserving methods are highly desirable, particularly in catalysis research.

Here we introduce operando hard X-ray spectrotomography applied to a complex emissions control process, Cu-SSZ-13 catalysed NH_3-SCR, on a washcoated monolithic catalyst. Using a dedicated sample environment for operando tomography, we combined XAS and X-ray CT for spatially- and energy-resolved 3D imaging at Cu K edge, coupled to quantitative catalytic performance data. Probing the catalyst under NH_3-SCR conditions from 200 to 400 °C revealed clear chemical gradients of Cu oxidation state and degree of NH_3 coordination within the Cu-SSZ-13 washcoat. Crucially, we show that direct semi-quantitative observation of chemical gradients as a function of temperature and washcoat structure is uniquely possible with operando spectrotomography. As demonstrated here for automotive catalysis, the method is applicable for a variety of technical catalysts and functional materials.

Results

Monolith Preparation and NH_3-SCR Reaction Conditions

Coated monolithic NH_3-SCR catalysts were prepared by washcoating Cu-SSZ-13 (1.8 wt.% Cu) onto a cordierite honeycomb substrate with square channels (~1.27 mm edge length). Single monolithic channels and channel corners (ca. 5 mm length) were carefully extracted using a razor blade, without damaging the washcoat, and placed

5

within the spectrotomography reactor (see also Supplementary Methods). Standard SCR conditions (1000 ppm NO, 1000 ppm NH_3, 7.8% O_2 in He, total flow 50 ml/min) were maintained while varying the temperature from 200 to 400 °C using hot air blowers over a period of 50 hours. Reference conditions were also measured, including 1000 ppm NH_3 in He (NH_3 only reference), and 1000 ppm NO with 7.8% O_2 in He (NO only reference). NO conversion and N_2 yield were analysed by a mass spectrometer positioned downstream from the reactor. The high gas hourly space velocity (GHSV) together with high gas bypass through the monolith channel void limited the NO conversion to approximately 10%. This allows the assumption of a relatively uniform gas composition throughout the catalyst bed (e.g. maximum possible gradient of NH_3 and NO from 1000 to 900 ppm along the reactor), and therefore an expected uniform composition of the catalyst in axial geometry.

Operando Spectrotomography of Cu-SSZ-13 Monolith

The spectrotomography setup designed for this study (Figure 1a, including X-ray transparent support rod for stability) was installed at microXAS beamline (Paul Scherrer Institut, see also Supplementary Methods). An X-ray beam in parallel geometry with a cross-section of around 1.5 * 1 mm and energy tuned around the Cu K absorption edge was used to acquire full-field projected images of the catalyst monolith. Collecting projection series at 51 different energy points from 8970 to 9010 eV, while rotating the sample through a 180° arc, enabled tomographic data reconstruction with a final 3D spatial resolution of 5 µm (see also Supplementary Methods). This combination of XAS and 3D imaging is denoted here as spectrotomography. The resulting data volume can be subdivided into cross-sectional images or slices, providing a 3D view of the sample interior. For example, a clear distinction between catalyst washcoat material and cordierite honeycomb could be

readily observed based on differing absorption contrast (Figure 1a and Figure 2a-b). Within each slice, each individual pixel consists of an independent X-ray absorption near edge structure (XANES) spectrum at Cu K edge (Figure 2c). In this way the active metal species could be probed and independently co-located in 3D within the entire technical catalyst under various operando conditions. Note that the pre-edge and edge features at the Cu K edge are strongly dependent on the oxidation state and particularly the geometry of Cu sites with different probability of 1s-3d and 1s-4p transitions[41,42].

As a result of this data collection strategy, distinct gradients in XANES intensity were observed under operando SCR conditions. These manifested in an approximately radial manner, centred on the innermost corner of the washcoat. The gradients were apparently linked to the washcoat thickness (see also Supplementary Discussion), or conversely the distance from the open gas stream in the surrounding capillary (Figure 1b). This effect was noticeable particularly at 8983 eV, correlating to the presence of an intense feature commonly observed in Cu(I) species, especially linear $Cu(NH_3)_2^+$ species or similar geometries due to allowed 1s-4p transitions[43]. The gradients were furthermore linked to temperature and most visible above 300 °C, correlating with NO conversions of 10 to 12% (Figure 1b). In contrast, at 200 °C the gradients were less pronounced, indicating a comparatively uniform state of Cu and lower NO conversion.

3D Spatially-Resolved XANES Fitting of Cu-SSZ-13 Washcoat

To explain the presence of these chemical gradients according to the current understanding of the NH_3-SCR mechanism, XANES fitting and analysis of the entire washcoat material was performed. Although this was possible on a per-pixel basis, several regions of interest (ROIs) were defined in order to improve spectral quality and facilitate image analysis (Figure 2b). XANES data was extracted in an approximately

radial manner starting from the thickest point of the washcoat at the honeycomb corner (ROI 1), to the washcoat exterior close to the gas stream (ROI 5) (Figure 2c). ROIs 1 through 5 therefore represent a chemical fingerprint of Cu oxidation state and coordination environment, correlated to increasing diffusion path lengths of reactant or product gas through the washcoat.

Operando spectrotomography experiments were performed under standard SCR conditions at T ≥ 200 °C, therefore the most relevant Cu species were considered to be Cu(I) with or without bonded NH_3, along with hydrated and dehydrated Cu(II)[10,13,44]. Due to their different oxidation state and geometry and thus different Cu 1s-4p transition probability, the XANES spectra of these copper species are clearly distinguishable by their form, particularly the feature at 8983 eV[10,43]. To map the distribution of specific Cu species in the washcoat, linear combination fitting of the measured XANES spectra was performed after ROI selection and normalisation (see also Supplementary Discussion and Supplementary Figure 4-9). The following four species were selected as references: Cu(I)*NH_3 corresponding to linear Cu(NH_3)$_2^+$; Cu(I) mostly without adsorbed ammonia; hydrated Cu(II) (five-coordinated); and dehydrated Cu(II) (three- or four-coordinated, the spectra of which are highly similar)[6,10,45]. For further information on selection and acquisition of reference data see Supplementary Discussion.

Influence of Reaction Temperature on Chemical Gradients

Operando spectrotomography enabled identification and co-localisation of active metal sites throughout the entire sample. To illustrate this, an identical orthogonal slice was initially selected from the tomography volumes to compare the gradients present at different reaction temperatures (Figure 3a-d). At 200 °C XANES fitting showed a

mixture of Cu(I) and Cu(II) coordinated with NH_3 in the washcoat (Figure 3a,e), while at the same time negligible NO conversion was recorded by mass spectrometry (Figure 1b) (see also Supplementary Discussion and Supplementary Figure 16). This data confirms that the adsorption rate of NH_3 in the washcoat was faster than the reaction rate. This led to an overall presence of NH_3, and most likely inhibition of the reaction due to strong adsorption of NH_3 at low temperature[9,11,12]. This inhibition effect was also described previously for iron-based zeolite SCR catalysts[46]. Notably, the outer ROIs (4-5) showed a gradual increase in the proportion of Cu(I) with adsorbed NH_3, compared to the more uniform composition of the inner washcoat (ROI 1-3) (Figure 3a,e). As reoxidation of Cu(I) to Cu(II) is considered to be a rate limiting step[4], the increased presence of Cu(I) at the washcoat exterior suggests that potential NH_3 inhibition effects were more significant there. At the same time, the washcoat interior experienced lower partial pressure of NO and NH_3 (due to reaction in the outer washcoat layer) and therefore lower degree of NH_3 inhibition. At 200 °C this likely resulted in a higher SCR rate towards the washcoat interior, producing relatively more Cu(II) species visible in the inner washcoat regions (ROI 1-3). This indicates that NO may have been partly consumed before reaching the inner washcoat (ROI 1-3), although N_2 detected by mass spectrometry was still negligible at this stage. Formation of water can also be expected during standard SCR, which at lower temperature (e.g. 200 °C) can compete with NH_3 for adsorption on Cu sites, resulting in a higher fraction of Cu(II) species[9]. Here due to low NO conversion at 200 °C only limited water formation was expected. We therefore can begin to assemble a consistent picture of the reaction steps occurring within the washcoat using operando spectrotomography.

On heating to 300 °C a clear and striking gradient in oxidation state became visible, with greatly decreased Cu(II) content moving from the inner corner (ROI 1) to the

9

washcoat exterior (ROI 5) (Figure 3b,f). The more apparent gradients in Cu speciation at 300 °C compared to 200 °C can be explained by the relatively higher global reaction rate at 300 °C (10% NO conversion), and the related reduced inhibitory effect of adsorbed NH_3 at higher temperature[9]. Since the same environmental conditions were applied to the entire monolith sample, differences in the observed chemical state must be due to an additional effect. The strong gradients observed at 300 °C can therefore be interpreted as a direct semi-quantitative visualisation of mass transport limitations of NH_3 and NO reactant gases to the washcoat interior. The presence of mass transport limitations is consistent with the increased formation of mainly Cu(I) species both with and without adsorbed NH_3 in the outermost washcoat region (ROI 5), i.e. within 20 μm of the open channel (Figure 3b,f). In effect, the greater the distance or diffusion length between a specific unit volume of the washcoat and the channel exterior, the less NO and NH_3 reaching the inner ROIs due to mass transport limitations, and therefore the lower the reaction rate which would lead to Cu(I) formation.

At higher temperatures of 350 °C (Figure 3c,g) to 400 °C (Figure 3d,h), NO conversions remained around 10%. According to previous studies, a local conversion maximum would be expected to be reached below 300 °C for a typical Cu-SSZ-13 catalyst[6,9]. The low maximum NO conversion (10%) observed here together with the absence of a significant increase in NO conversion between 300 to 400 °C is also consistent with the presence of severe mass transport limitations under the chosen gas flow conditions. Significant portions of the catalyst washcoat were expected not to reach 100 % conversion due to mass transport limitations of reactants to the active copper sites, while the relative temperature increase therefore had no significant effect on activity in these regions. At 350 to 400 °C the Cu(II) gradient first observed at lower

temperatures was again clearly visible (Figure 3a,b). However in addition, the different local ammonia concentration at 350 °C compared to 400 °C also caused more apparent changes in XANES spectra (Figure 3c,d), with increased proportion of Cu(I)*NH$_3$ moving towards the washcoat exterior (ROI 1 to ROI 5). It is known that Cu-SSZ-13 SCR catalysts have a local minimum in NO conversion at around 350 °C, the so-called seagull-shaped conversion curve[47], which is likely to coincide with more unconverted absorbed ammonia on Cu(I) species[9,14,48]. This is supported in spectrotomography by the absence of Cu(I) without ammonia at 350 °C (Figure 3c,g) indicating total coverage of Cu(I)*NH$_3$. In contrast, Cu(I) without ammonia was observed previously at 300 °C (Figure 3b,f) and again at 400 °C (Figure 3d,h). At temperatures of 350 °C and above water is known to desorb from the zeolite, while competition between water and NH$_3$ for adsorption sites was previously found to be minimal[9].

Following the apparent local activity minimum at 350 °C, on heating to 400 °C a complete and unambiguous reduction of Cu(II) to Cu(I) species (with and without NH$_3$) was observed in the outer areas of the washcoat ROI 4-5 (Figure 3h). Due to high SCR rate, Cu(I)*NH$_3$ was observed predominantly in the outer region (ROI 5) with the highest local NH$_3$ concentration. On the other hand, the higher Cu(II) amount in the inner regions (ROI 1-2) is caused by the lower NO concentration and thus lower SCR rate there. This indicates depletion of NO and NH$_3$ already in the outer regions, combined with relatively slow reactant diffusion to the washcoat interior (mass transport limitations). Notably, no gradients were observed under the reference conditions measured (1000 ppm NH$_3$ only, and 1000 ppm NO with 7.8% O$_2$) but rather a uniform composition of Cu(I)*NH$_3$ and Cu(II) were observed, respectively (see Supplementary Discussion and Supplementary Figure 14). This proves the gradients

observed during NH$_3$-SCR are real observations and not a result of artefacts from data acquisition or tomographic reconstruction.

Insight into the NH3-SCR Mechanism on Structured Catalysts

The use of our operando spectrotomography method offered detailed insights into a Cu-SSZ-13 washcoated monolith catalyst at work. For the first time, the consequences of mass transport limitations could be visualised in the form of chemical gradients in the structure of the Cu sites in Cu-SSZ-13. A stable NO conversion and N$_2$ yield were recorded at 300 °C and above (Figure 1b) (at 200 °C low conversion was observed, see also Supplementary Discussion), proving that the catalyst was captured in an active state and allowing structure and activity to be connected. This makes it possible to reinterpret earlier literature studies with differing explanations of the copper active species. At relatively low temperatures of 200 °C, Cu(I)*NH$_3$ was present rather uniformly in the entire washcoat. This is consistent with the known strong inhibitory effect of NH$_3$ up to 300 °C, which is weaker at higher temperatures[9]. However, in contrast to other studies[3], Cu(I)*NH$_3$ or Cu(I) species were also found between 300 and 400 °C. In addition, complete reduction of the most active washcoat exterior regions to Cu(I) was observed at 400 °C. This is consistent with most currently proposed reaction mechanisms, which specify re-oxidation of Cu(I) to Cu(II) as one rate determining step at both low and elevated temperatures[4,9], coupled here with the presence of diffusion limitations to the inner washcoat. The latter may also explain why in studies where mass transport is not optimal (e.g. model disc-shaped catalysts) Cu(II) has been observed as the most abundant species at elevated temperatures[3,45]. The gradients observed were also investigated as a function of washcoat thickness by studying different vertical positions of the monolith. Notably for thinner sections Cu(I)

was completely absent in favour of Cu(I)*NH$_3$ (see Supplementary Discussion), reinforcing that sample thickness had a strong influence on NH$_3$ adsorption under the chosen conditions, and that operando spectrotomography is sensitive enough to detect these effects.

Operando spectrotomography not only revealed that NH$_3$-SCR occurs non-uniformly within structured catalysts, but crucially could identify and locate specific chemical gradients linked to temperature and catalyst shape. This is in contrast to studies of NH$_3$-SCR on powder catalysts with conventional bulk XAS, where spatial variation and discrimination of Cu(I)*NH$_3$, Cu(I) and Cu(II) at different radial positions in the catalyst bed is physically not possible. A level of caution is therefore needed when interpreting results of operando studies on model systems. Without consideration of spatiotemporal effects or spatially-resolved characterisation tools, such studies may not be representative of the technical application. Furthermore, it should be noted that conventional X-ray tomography either ex situ or at a single energy cannot produce the results shown here. An operando energy-resolved and spatially-resolved tomographic approach with quantitative activity data is absolutely essential to confirm the reaction is occurring, to probe the chemical state (e.g. using XAS), and to confirm the presence of gradients due to mass transport effects (rather than e.g. insufficient supply of reactants, see also Supplementary Note 1).

Conclusions

We demonstrate operando hard X-ray spectrotomography with XANES contrast as an effective characterisation tool which can simultaneously perform spatially- and energy-resolved 3D imaging, and identification of chemical states with μm-scale resolution using XAS. It is applicable to non-model catalyst systems under operando conditions,

combined with quantitative catalytic performance data. Applying this method to NH_3-SCR over Cu-SSZ-13 washcoated monolith catalysts provides not only conclusive evidence of chemical gradients in Cu oxidation state and coordination environment resulting from mass transport limitations in the catalyst washcoat, but demonstrates the potential to directly and semi-quantitatively image such gradients as a function of temperature and washcoat shape or thickness. Effectively, this enables observation of structure-activity relationships in complex heterogeneous catalytic systems. The ability to visualise the effects of mass transport limitations in this way can improve our understanding of NH_3-SCR in technical systems and clarify the different observations in literature with respect to the reaction mechanism. However, performing operando tomographic imaging alone is not sufficient to investigate catalytic active sites during NH_3-SCR, rather a combined spectroscopic analysis such as XANES is required. The method is directly applicable to other transition or noble metal catalysed emission control processes, and can be used to probe structure-activity relationships in 3D space, with relevance to catalyst synthesis, structure optimisation, and kinetic and multi-scale modelling.

Methods

Sample Preparation

The Cu-SSZ-13 zeolite catalyst was prepared by liquid ion exchange of commercially purchased NH_4-SSZ-13 with a Si/Al ratio of 14. Cu-exchange was carried out with a 0.005 M aqueous $Cu(OAc)_2$ solution at room temperature for 24 h, after which the suspension was filtered, washed with deionised water, and dried at 80 °C (for details see reference[6]). Afterwards the dried powder was calcined at 550 °C for 8 h in static air. X-ray fluorescence analysis confirmed a Cu loading of 1.8 wt%. A slurry of the

calcined catalyst was prepared by mixing 5.43 g Cu-SSZ-13 with 45 mL deionised water and 1.43 g binder (Ludox AS-40, colloidal silica solution) in a ball mill. The catalyst powder was applied to a rectangular cordierite honeycomb (400 cpsi cell density) 1 cm wide and 2 cm long by dip coating and drying with a hot air blower. This process was repeated until a total amount of 1.53 g/cm³ washcoat was applied to the honeycomb. To finalise the preparation of the honeycomb it was calcined for 8 h at 550 °C in static air.

Operando Spectrotomography Setup

The key to the operando spectrotomography measurements was the development of a dedicated sample holder to combine operando spectroscopy and hard X-ray microtomography (see also Supplementary Methods, Supplementary Note 1, and Supplementary Figure 1-2). The sample holder consists of a quartz capillary (in this case 1 mm diameter) as reactor, mounted vertically on a precision rotation stage (PRS-110, PI, Germany). The capillary was enclosed using epoxy glue in a support bracket ensuring free rotation, with gas connections at the top and bottom. A glassy carbon rod (HTW Hochtemperatur-Werkstoffe GmbH, Germany) was integrated to support the weight of the stainless-steel gas connections and reduce tension on the quartz capillary. The support rod is virtually transparent to hard X-rays at Cu K edge (8.979 keV), which was a key experimental advance in this study, and did not significantly impact the tomography scans or the data reconstruction process (see also Supplementary Methods and Supplementary Figure 3). The setup is capable of maintaining micrometer precision stability across a 180° rotational range required for tomography. The gas dosing system consisted of mass flow controllers (Bronkhorst El-Flow, Netherlands), while the products were analysed by a mass spectrometer (Pfeiffer Vacuum OmniStar GSD-320, Germany) positioned downstream from the reactor. Two

gas blowers (Leister LE Mini, Switzerland) were positioned on opposite sides of the capillary to provide even radial heat distribution to the sample. The gas blowers were controlled using custom LabVIEW scripts. Temperature was calibrated prior to the measurements and checked at several different points during the measurements using a type K thermocouple positioned close to the capillary exterior. The setup therefore allows operando tomography measurements together with quantitative product sampling in a controlled gas and temperature environment. The setup is portable and can be implemented at different microtomography beamlines (see Supplementary Methods, Supplementary Note 1, and Supplementary Discussion).

Full-field XANES Spectrotomography

A single monolith channel was cut out from the honeycomb structure with a razor and placed inside the spectrotomography sample holder. Measurements were performed at the microXAS beamline of the Swiss Light Source (Paul Scherrer Institute, Switzerland), which is an insertion-device based beamline, using an undulator (U19) that serves as radiation source. The incident full-field beam was tuned to a slightly larger size than the lateral cross section of the capillary, covering an area of approximately 1.5 * 1 mm^2. The beam size in the horizontal direction was tuned with a toroidal mirror placed at about 17 meters from the source, and about 23 meters from the sample position. A fixed-exit double crystal monochromator (DCM) using a Si(111) crystal was used for energy selection of the X-rays. Full-field projections were recorded using a YAG:Ce-doped scintillator coupled to 10-fold objective and a CCD camera (pco. 2000, 2048 × 2048 pixels, 7.4 um pixel size, 6 e− rms at 10 MHz). Flat-field projections (equivalent to incident intensity, I_0) were recorded regularly during the measurement by moving the sample out of the beam position. 2D full-field projections of the sample were recorded across a rotational range of 180° at a single energy, to

generate one tomogram. These projection series were repeated in sequence at a total of 51 energy points from 8.95 to 9.22 keV with variable step size (see Supplementary Table 1), to produce Cu K edge XANES data at each sampling point (detector pixel). The acquisition time for a complete projection series at all energy points was approximately 13 hours (see Supplementary Note 1, Supplementary Methods, and Supplementary Discussion.

Seven different measurement conditions were applied during the spectrotomography measurements, including an ex situ scan under ambient conditions, and sequential measurements under model standard SCR conditions (1000 ppm NO, 1000 ppm NH_3, 7.8% O_2 in He, total flow 50 ml/min) at four temperature points (200, 300, 350 and 400 °C). Two reference measurements were also performed using: 1000 ppm NH_3; and 1000 ppm NO with 7.8% O_2 in He, in both cases at 200 °C. Before beginning spectrotomography scans, the sample was allowed to equilibrate for a minimum of 1 hour under each condition. In the case of the SCR measurements, these were performed only after stabilisation of the NO and N_2 signals as observed by mass spectrometry, to ensure steady state operation during the long tomography scans. The mass spectrometry data for NO and N_2 are shown and discussed in Supplementary Discussion and Supplementary Figure 16. Water was not dosed as part of the standard SCR feed due to the absence of heated gas lines and the small uniform heating zone of the gas blowers (see Supplementary Methods). Formed water traces are expected to be relatively uniform along the reactor axis, due to low overall NO conversion at 200 to 400 °C.

Spectrotomography Data Processing

A full description of the data processing procedure can be found in Supplementary Methods and Supplementary Figure 3. The raw spectrotomography data consisted of full-field 2D projection series across a 180° rotation range. Each projection series contained the carbon support rod at several angles, which was firstly subtracted as a background feature to produce corrected projection series containing only the sample and capillary. To compensate for fluctuation in beam intensity and sample movement, alignment was performed first for energy series at each projection angle, followed by a second alignment of projection series at each rotational angle. Individual sinograms were then generated for each horizontal line on the aligned projection series at each energy point. The sinograms were then reconstructed using the simultaneous iterative reconstruction algorithm of the ASTRA Python library[49]. This resulting 3D volumes provide a non-invasive 3D spatially-resolved view of the monolith interior, resolved both by energy and X-ray absorbance, whereby each individual sampling point contains a full XANES spectrum. The resulting datasets can be considered multidimensional with at least 5D, even before considering time, temperature, and catalytic activity as additional parameters.

Linear Combination Analysis of ROI-Averaged XANES Spectra

Linear combination analysis (LCA) of the XANES spectra in the region from 8979.5 eV to 8992.5 eV (rising edge region) was used to determine the state of Cu in the corresponding parts of the washcoat (see Supplementary Table 2), (for further information on references see Supplementary Discussion). The spectra extracted were an average of the individual pixel contributions contained within each ROI, including 3132, 8559, 8181, 8919 and 3786 pixels for ROIs 1 to 5, respectively. Prior to LCA, the acquired XANES spectra in each region of interest were normalised using the pre-edge region from -33 to -3 eV and post-edge region from +15 to +27 eV. Such short

ranges were chosen due to limited density of scanning points (51 in total from 8950 to 9220 eV) as a result of time constraints. ATHENA software from the IFFEFIT package was used for data analysis[50]. As references, the spectra of hydrated Cu(II) (which was not required and no effect on the fit results at 350°C and 400°C, in accordance to previous work[10]) and dehydrated Cu(II) species were used (spectra of Cu(II) with or without adsorbed ammonia are too similar to distinguish in our case)[14]. It is important to note that the quality of fitting for ROIs with higher Cu(II) content was generally worse than for other species. This most likely comes from the presence of Cu(II) with adsorbed NH_3 species for which a reference was not available, due to similarity of their spectra to other Cu(II) references[14]. Cu(I)*NH_3 and Cu(I) references were obtained from operando QEXAFS data previously measured on a powder Cu-SSZ-13 catalyst using multivariate curve resolution – alternating least squares method (MCR-ALS, see Supplementary Discussion)[9,10]. To check the fitting procedure for robustness, we also performed fits using internal reference spectra obtained in NH_3 (as a reference of Cu(I)*NH_3) and in NO+O_2 (as a reference of Cu(II)) at 200 °C, with this approach leading to the same observed trends (see Supplementary Discussion and Supplementary Figure 14). The reference spectra were normalised in the same way as the XANES spectrotomography data. During fitting, energy adjustment within 1 eV was allowed for the experimental spectra, while the energy scale of the reference spectra was fixed. The energy adjustment was performed because the references were measured by standard transmission XAS together with Cu foil reference sample for proper energy scale calibration, while for the spectrotomography data the energy scale stability could only be measured at regular intervals between rotational series. In addition, the energy resolution between conventional XAS and spectrotomography may be slightly different due to variation in instrumentation and beam size. Altogether, the fits included 13 datapoints and 3-4 fitted variables (2-3 for weights and 1 for the

19

energy shift). The misfit (ρ) is defined as $\Sigma(\text{data-fit})^2 / \Sigma(\text{data})^2$ and the error bars for the calculated weights are within ± 0.15. Fitted spectra and residuals are shown in Supplementary Discussion and Supplementary Figure 4-9.

Data Availability Statement

Raw data were generated at the Swiss Light Source of the Paul Scherrer Institut (Switzerland). The collected and cleaned imaging data before tomographic reconstruction that support the findings of this study are stored in KITopen, the central repository of Karlsruhe Institute of Technology, and are freely available with the following DOIs: 200 °C dataset doi:10.5445/IR/1000122874, 300 °C dataset doi:10.5445/IR/1000122890, 350 °C dataset doi:10.5445/IR/1000122892, 400 °C dataset doi:10.5445/IR/1000122893, NH_3 reference dataset doi:10.5445/IR/1000122894, NO reference dataset doi:10.5445/IR/1000122895. Additional data including reconstructed and treated spectrotomography datasets are available from the authors upon reasonable request. Source data for Figures 1, 2 and 3 are provided with the paper.

References

1   Beale, A. M., Gao, F., Lezcano-Gonzalez, I., Peden, C. H. F. & Szanyi, J. Recent advances in automotive catalysis for NOx emission control by small-pore microporous materials. *Chem. Soc. Rev.* **44**, 7371-7405 (2015).
2   Borfecchia, E. *et al.* Cu-CHA – a model system for applied selective redox catalysis. *Chem. Soc. Rev.* **47**, 8097-8133 (2018).
3   Lomachenko, K. A. *et al.* The Cu-CHA deNOx Catalyst in Action: Temperature-Dependent NH3-Assisted Selective Catalytic Reduction Monitored by Operando XAS and XES. *J. Am. Chem. Soc.* **138**, 12025-12028 (2016).
4   Janssens, T. V. W. *et al.* A Consistent Reaction Scheme for the Selective Catalytic Reduction of Nitrogen Oxides with Ammonia. *ACS Catal.* **5**, 2832-2845 (2015).
5   Bates, S. A. *et al.* Identification of the active Cu site in standard selective catalytic reduction with ammonia on Cu-SSZ-13. *J. Catal.* **312**, 87-97 (2014).
6   Günter, T. *et al.* Structural snapshots of the SCR reaction mechanism on Cu-SSZ-13. *Chem. Commun.* **51**, 9227-9230 (2015).
7   Günter, T. *et al.* The SCR of NOx with NH3 Examined by Novel X-ray Emission and X-ray Absorption Methods. *Top. Catal.* **59**, 866-874 (2016).
8   Paolucci, C. *et al.* Dynamic multinuclear sites formed by mobilized copper ions in NOx selective catalytic reduction. *Science* **357**, 898-903 (2017).

9   Fahami, A. R. *et al.* The dynamic nature of Cu sites in Cu-SSZ-13 and the origin of the seagull NOx conversion profile during NH3-SCR. *React. Chem. Eng.* **4**, 1000-1018 (2019).

10   Kerkeni, B. *et al.* Copper Coordination to Water and Ammonia in CuII-Exchanged SSZ-13: Atomistic Insights from DFT Calculations and in Situ XAS Experiments. *J. Phys. Chem. C.* **122**, 16741-16755 (2018).

11   Auvray, X. *et al.* Local ammonia storage and ammonia inhibition in a monolithic copper-beta zeolite SCR catalyst. *Appl. Catal. B.* **126**, 144-152 (2012).

12   Marberger, A. *et al.* Time-resolved copper speciation during selective catalytic reduction of NO on Cu-SSZ-13. *Nat. Catal.* **1**, 221-227 (2018).

13   Greenaway, A. G. *et al.* Detection of key transient Cu intermediates in SSZ-13 during NH3-SCR deNOx by modulation excitation IR spectroscopy. *Chem. Sci.* **11**, 447-455 (2020).

14   Clark, A. H. *et al.* Selective Catalytic Reduction of NO with NH3 on Cu-SSZ-13: Deciphering the Low and High-temperature Rate-limiting Steps by Transient XAS Experiments. *ChemCatChem* **12**, 1429-1435 (2020).

15   Grunwaldt, J.-D., Wagner, J. B. & Dunin-Borkowski, R. E. Imaging Catalysts at Work: A Hierarchical Approach from the Macro- to the Meso- and Nano-scale. *ChemCatChem* **5**, 62-80 (2013).

16   Gänzler, A. M. *et al.* Unravelling the Different Reaction Pathways for Low Temperature CO Oxidation on Pt/CeO2 and Pt/Al2O3 by Spatially Resolved Structure–Activity Correlations. *J. Phys. Chem. Lett.* **10**, 7698-7705 (2019).

17   Andrews, J. C. & Weckhuysen, B. M. Hard X-ray Spectroscopic Nano-Imaging of Hierarchical Functional Materials at Work. *ChemPhysChem* **14**, 3655-3666 (2013).

18   Goguet, A., Stewart, C., Touitou, J. & Morgan, K. in *Advances in Chemical Engineering* Vol. 50 131-160 (Elsevier, 2017).

19   Dong, Y., Korup, O., Gerdts, J., Roldán Cuenya, B. & Horn, R. Microtomography-based CFD modeling of a fixed-bed reactor with an open-cell foam monolith and experimental verification by reactor profile measurements. *Chem. Eng. J.* **353**, 176-188 (2018).

20   Jurtz, N., Kraume, M. & Wehinger, G. D. Advances in fixed-bed reactor modeling using particle-resolved computational fluid dynamics (CFD). *Rev. Chem. Eng.* **35**, 139-190 (2019).

21   Buurmans, I. L. C. & Weckhuysen, B. M. Heterogeneities of individual catalyst particles in space and time as monitored by spectroscopy. *Nat. Chem.* **4**, 873-886 (2012).

22   Urakawa, A. & Baiker, A. Space-resolved profiling relevant in heterogeneous catalysis. *Top. Catal.* **52**, 1312-1322 (2009).

23   Beale, A. M., Jacques, S. D. M. & Weckhuysen, B. M. Chemical imaging of catalytic solids with synchrotron radiation. *Chem. Soc. Rev.* **39**, 4656-4672 (2010).

24   Sanchez, D. F. *et al.* 2D/3D Microanalysis by Energy Dispersive X-ray Absorption Spectroscopy Tomography. *Sci. Rep.* **7**, 16453 (2017).

25   Ihli, J. *et al.* A three-dimensional view of structural changes caused by deactivation of fluid catalytic cracking catalysts. *Nat. Commun.* **8**, 809 (2017).

26   Sheppard, T. L. *et al.* In Situ Multimodal 3D Chemical Imaging of a Hierarchically Structured Core@Shell Catalyst. *J. Am. Chem. Soc.* **139**, 7855-7863 (2017).

27   Weker, J. N., Huang, X. & Toney, M. F. In situ X-ray-based imaging of nano materials. *Curr. Op. Chem. Eng.* **12**, 14-21 (2016).

28   Price, S. W. T. *et al.* Chemical imaging of single catalyst particles with scanning µ-XANES-CT and µ-XRF-CT. *Phys. Chem. Chem. Phys.* **17**, 521-529 (2015).

29   Becher, J. *et al.* Mapping the Pore Architecture of Structured Catalyst Monoliths from Nanometer to Centimeter Scale with Electron and X-ray Tomographies. *J. Phys. Chem. C.* **123**, 25197-25208 (2019).

30   Hofmann, G. *et al.* Aging of a Pt/Al2O3 exhaust gas catalyst monitored by quasi in situ X-ray micro computed tomography. *RSC Adv.* **5**, 6893-6905 (2015).

31   Meirer, F. *et al.* Mapping Metals Incorporation of a Whole Single Catalyst Particle Using Element Specific X-ray Nanotomography. *J. Am. Chem. Soc.* **137**, 102-105 (2015).

32   Bossers, K. W. *et al.* Correlated X-ray Ptychography and Fluorescence Nano-Tomography on the Fragmentation Behavior of an Individual Catalyst Particle during the Early Stages of Olefin Polymerization. *J. Am. Chem. Soc.* **142**, 3691-3695 (2020).

33   Price, S. W. T. *et al.* Chemical imaging of Fischer-Tropsch catalysts under operating conditions. *Sci. Adv.* **3**, e1602838 (2017).

34   Senecal, P. *et al.* Real-Time Scattering-Contrast Imaging of a Supported Cobalt-Based Catalyst Body during Activation and Fischer–Tropsch Synthesis Revealing Spatial Dependence of Particle Size and Phase on Catalytic Properties. *ACS Catal.* **7**, 2284-2293 (2017).

35   Cats, K. *et al.* Active phase distribution changes within a catalyst particle during Fischer–Tropsch synthesis as revealed by multi-scale microscopy. *Catal. Sci. Technol.* **6**, 4438-4449 (2016).

36   Matras, D. *et al.* Operando and Postreaction Diffraction Imaging of the La–Sr/CaO Catalyst in the Oxidative Coupling of Methane Reaction. *J. Phys. Chem. C.* **123**, 1751-1760 (2019).

37   Vamvakeros, A. *et al.* Real time chemical imaging of a working catalytic membrane reactor during oxidative coupling of methane. *Chem. Commun.* **51**, 12752-12755 (2015).

38   Vamvakeros, A. *et al.* 5D operando tomographic diffraction imaging of a catalyst bed. *Nat. Commun.* **9**, 4751 (2018).

39   Schmidt, J. E., Oord, R., Guo, W., Poplawsky, J. D. & Weckhuysen, B. M. Nanoscale tomography reveals the deactivation of automotive copper-exchanged zeolite catalysts. *Nat. Commun.* **8**, 1666 (2017).

40   Schmidt, J. E. *et al.* Probing the Location and Speciation of Elements in Zeolites with Correlated Atom Probe Tomography and Scanning Transmission X-Ray Microscopy. *ChemCatChem* **11**, 488-494 (2019).

41   Paolucci, C. *et al.* Isolation of the Copper Redox Steps in the Standard Selective Catalytic Reduction on Cu-SSZ-13. *Angew. Chem. Int. Ed.* **53**, 11828-11833 (2014).

42   Alayon, E. M. C., Nachtegaal, M., Kleymenov, E. & van Bokhoven, J. A. Determination of the electronic and geometric structure of Cu sites during methane conversion over Cu-MOR with X-ray absorption spectroscopy. *Micro. Meso. Mater.* **166**, 131-136 (2013).

43   Zhang, R. & McEwen, J.-S. Local Environment Sensitivity of the Cu K-Edge XANES Features in Cu-SSZ-13: Analysis from First-Principles. *J. Phys. Chem. Lett.* **9**, 3035-3042 (2018).

44   Bendrich, M., Scheuer, A., Hayes, R. E. & Votsmeier, M. Unified mechanistic model for Standard SCR, Fast SCR, and NO2 SCR over a copper chabazite catalyst. *Appl. Catal. B.* **222**, 76-87 (2018).

45   Giordanino, F. *et al.* Interaction of NH3 with Cu-SSZ-13 Catalyst: A Complementary FTIR, XANES, and XES Study. *J. Phys. Chem. Lett.* **5**, 1552-1559 (2014).

46   Doronkin, D. E. *et al.* Operando Spatially- and Time-Resolved XAS Study on Zeolite Catalysts for Selective Catalytic Reduction of NOx by NH3. *J. Phys. Chem. C.* **118**, 10204-10212 (2014).

47   Gao, F., Mei, D., Wang, Y., Szanyi, J. & Peden, C. H. F. Selective Catalytic Reduction over Cu/SSZ-13: Linking Homo- and Heterogeneous Catalysis. *J. Am. Chem. Soc.* **139**, 4935-4942 (2017).

48   Gao, F. *et al.* Understanding ammonia selective catalytic reduction kinetics over Cu/SSZ-13 from motion of the Cu ions. *J. Catal.* **319**, 1-14 (2014).

49   van Aarle, W. *et al.* Fast and flexible X-ray tomography using the ASTRA toolbox. *Opt. Express* **24**, 25129-25147 (2016).

50   Ravel, B. & Newville, M. ATHENA, ARTEMIS, HEPHAESTUS: data analysis for X-ray absorption spectroscopy using IFEFFIT. *J. Synchrotron Radiat.* **12**, 537-541 (2005).

Acknowledgements

Author Contributions

T.L.S., D.M.M., D.E.D. and J-D.G. conceived and designed the experiments. J.B. and T.L.S. designed the spectrotomography setup. J.B. and D.Z. synthesised the materials. All authors contributed to preparation of beamtime proposals for access to synchrotron radiation, performed the experiments and acquired the data. D.F.S. and J.B. prepared code for processing of the raw data. J.B., D.F.S., D.E.D. and T.L.S performed analysis of the processed data, and with J-D.G. interpreted the data. J.B., T.L.S. and D.E.D. drafted the manuscript, and all authors contributed to revise the manuscript. J-D.G. and T.L.S. were responsible for acquisition of funding.

Competing Interests

The authors declare no competing interests.

Figures:
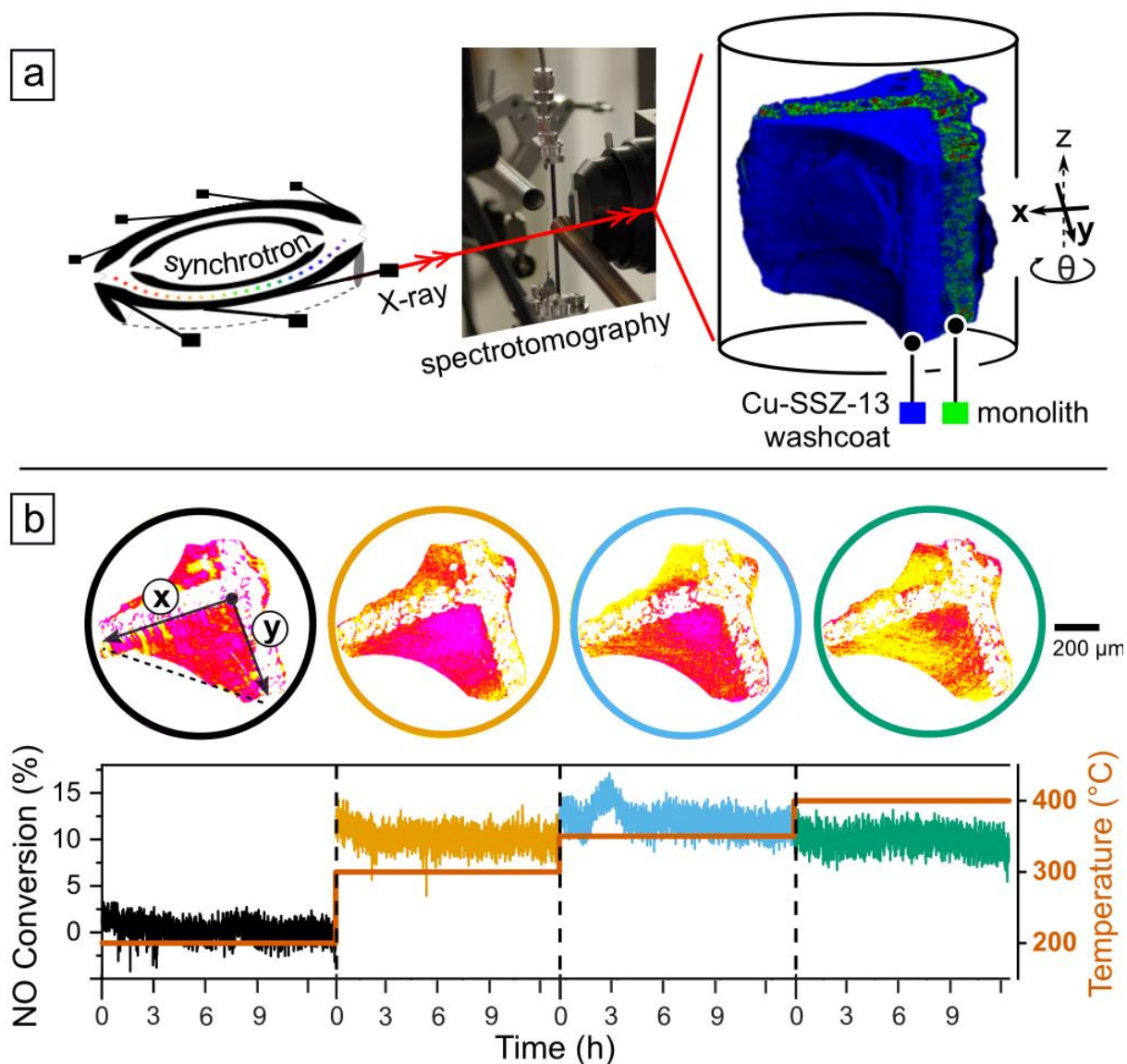
Figure 1 Operando spectrotomography of a Cu-SSZ-13 catalyst at work.

(a) Sketch of the operando spectrotomography experiment at microXAS beamline and tomography rendering of the Cu-SSZ-13 washcoated catalyst; (b) orthogonal raw data slices of the catalyst under model SCR conditions – artificially enhanced contrast depicting Cu XANES spectrum intensity at 8983 eV (for illustration and not normalised between datasets) - with truncated mass spectrometry data showing NO conversion during tomography scans at each temperature condition (zero is the time at which a tomography scan was started).

Figure 2 **3D view of the chemical gradient in a Cu-SSZ-13 washcoat.**
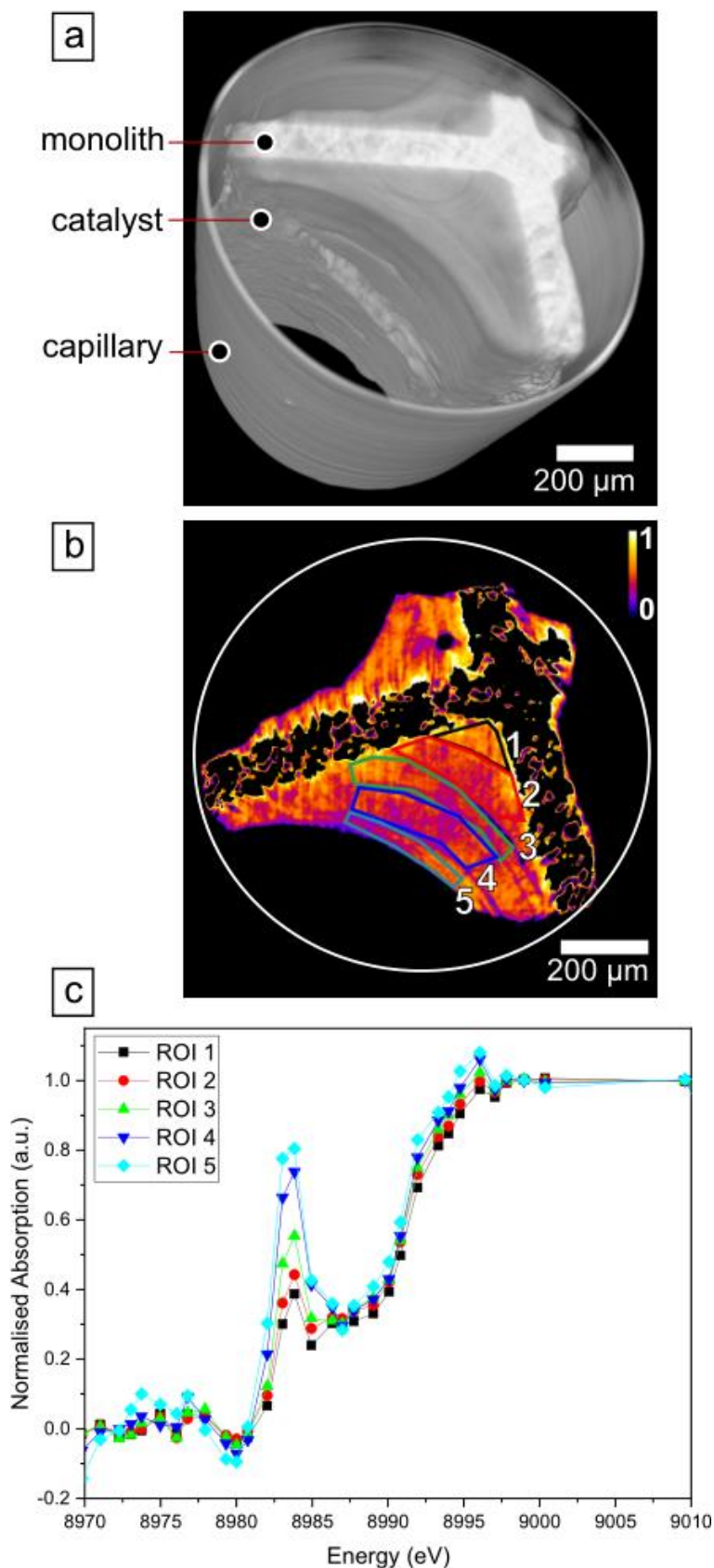
(a) tomography reconstruction of the entire monolith sample inside a 1 mm quartz capillary under SCR conditions; (b) orthogonal slice of the catalyst measured under SCR conditions at 350 °C - colour code depicts the intensity of the XANES feature at 8983 eV, showing the area of interest in ROIs 1-5 – cordierite monolith was thresholded and masked and did not affect the washcoat analysis; (c) average normalised XANES spectra from voxels within ROIs 1-5, corresponding with washcoat interior to exterior.
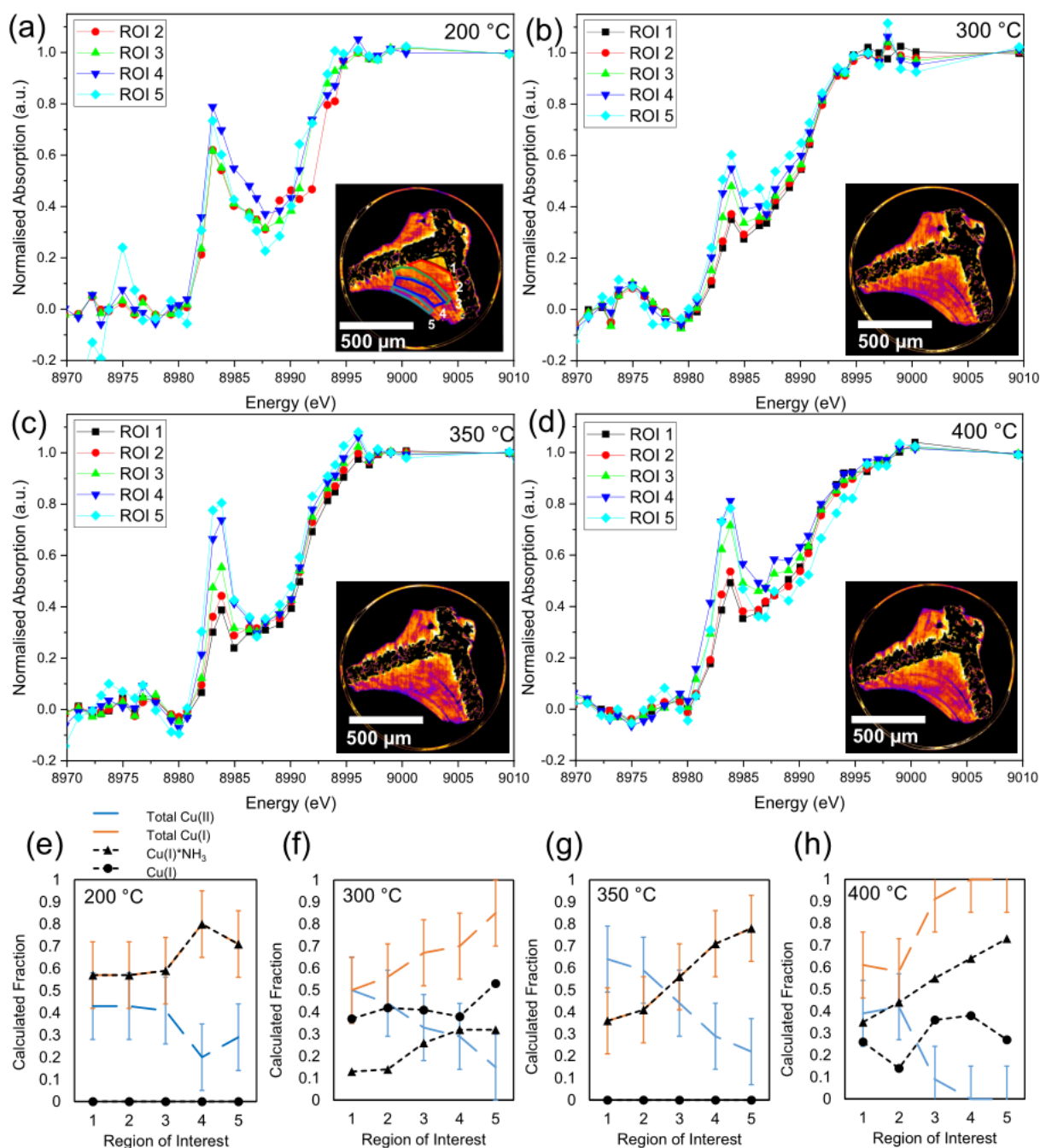
Figure 3 **Revealing the chemical state of Cu in a Cu-SSZ-13 washcoat.**

(a-d) Normalised Cu K edge XANES spectra in an identical sample slice at: (a) 200 °C; (b) 300 °C; (c) 350 °C; (d) 400 °C, showing visible gradients of the feature at 8983 eV from ROIs 1 to 5 (inset – fitted slice with colour corresponding to intensity of the XANES feature at 8983 eV). (e-h) Fitted fractions of Cu(I), Cu(I)*NH$_3$ and Cu(II) in the XANES spectra at: (e) 200 °C; (f) 300 °C; (g) 350 °C; (h) 400 °C showing gradients from ROIs 1 to 5. Error bars represent the maximum uncertainty reported by the Linear Combination Analysis subroutine of the Athena 0.8.056 software package.

Chemical gradients in automotive Cu-SSZ-13 catalysts for NOx removal revealed by operando X-ray spectrotomography

Johannes Becher[1], Dario Ferreira Sanchez[2], Dmitry E. Doronkin[1,3], Deniz Zengel[1], Debora Motta Meira[4,†], Sakura Pascarelli[4,‡], Jan-Dierk Grunwaldt[1,3,*], Thomas L. Sheppard[1,3,*]

[1] Institute for Chemical Technology and Polymer Chemistry (ITCP), Karlsruhe Institute of Technology (KIT), Engesserstr. 20, 76131 Karlsruhe, Germany

[2] Paul Scherrer Institut (PSI), 5232 Villigen, Switzerland

[3] Institute of Catalysis Research and Technology (IKFT), Karlsruhe Institute of Technology (KIT), Hermann-von-Helmholtz Platz 1, 76344 Eggenstein-Leopoldshafen, Germany

[4] European Synchrotron Radiation Facility (ESRF), 71 Avenue des Martyrs, 38000 Grenoble, France

†Current affiliation: CLS@APS Sector 20, Advanced Photon Source, Argonne National Laboratory, 9700 S. Cass Avenue, Argonne, IL 60439, USA; Canadian Light Source Inc., 44 Innovation Boulevard, Saskatoon, Saskatchewan S7N 2V3, Canada

‡Current affiliation: European XFEL GmbH, Holzkoppel 4, 22869 Schenefeld, Germany

Corresponding Authors: thomas.sheppard@kit.edu, grunwaldt@kit.edu

Contents

Supplementary Methods

Operando Spectrotomography Apparatus

The *operando* spectrotomography setup as shown in Supplementary Figure 1 consists of the following main components:

- Capillary sample holder (1 mm in the current work, other dimensions possible)
- Glassy carbon support rod (3 mm in the current work, other configurations possible) – this was key to supporting the setup, allowing use of X-ray transmission and *operando* infrastructure
- Stabilising bracket with integrated stainless-steel gas fittings
- Goniometer plate for vertical alignment
- X,Y manual stages for centre of rotation alignment
- Dual gas blowers for uniformly distributed heating
- A mass spectrometer positioned downstream of the reactor (not shown)
- Gas dosing system and temperature control system (not shown)
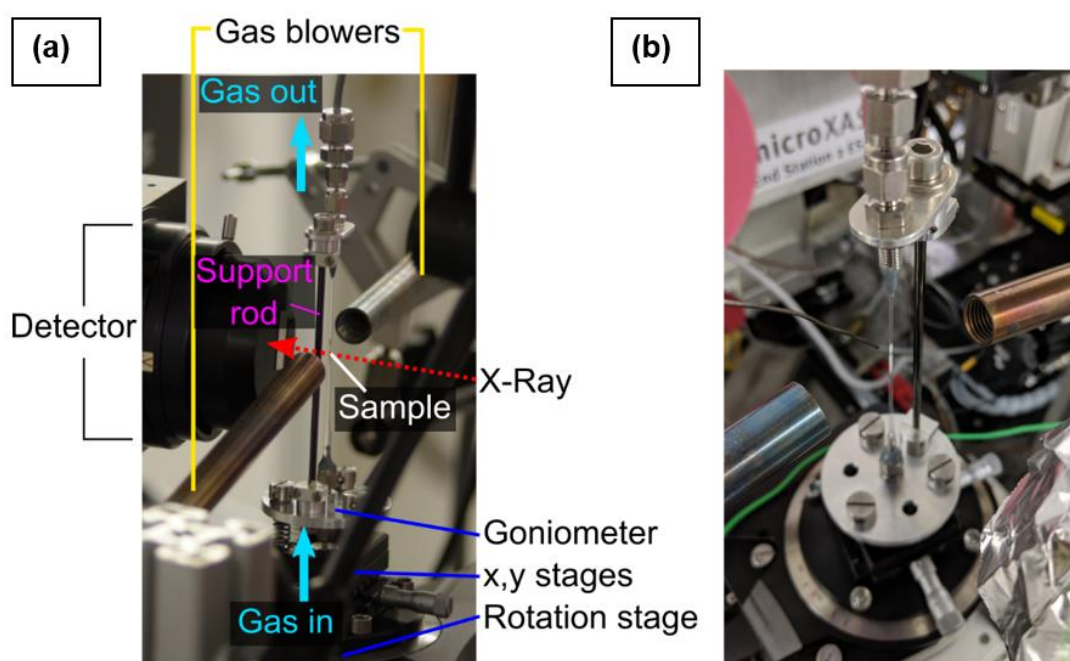
Supplementary Figure 1 – the *operando* spectrotomography setup installed at microXAS beamline of the Paul Scherrer Institut (Villigen, Switzerland): (a) during sample alignment; (b) during temperature calibration with external portable thermocouples, where the detector faceplate was partly wrapped in aluminium foil as a heat shield (right).
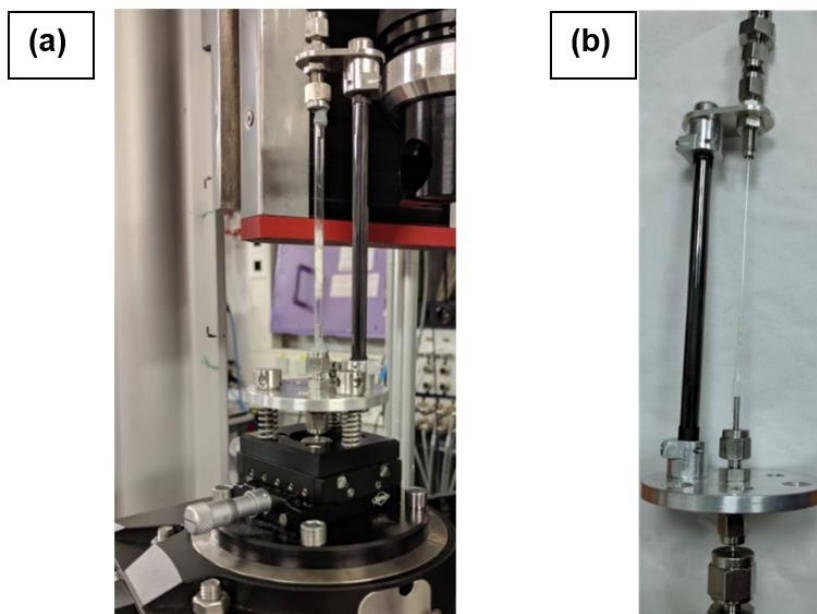
Supplementary Figure 2 – the *operando* spectrotomography setup showing: (a) the complete sample holder installed at beamline ID24 of the ESRF (Grenoble, France); (b) the isolated capillary and support bracket during sample preparation (right).

The *operando* spectrotomography setup is portable and can be installed at various spectroscopy and microtomography beamlines, as shown in Supplementary Figure 1 and Supplementary Figure 2. A typical workflow includes selecting the appropriate capillary size (e.g. 1-3 mm) and sample type (e.g. structured sample, powder) for the desired catalytic process and conditions (e.g. space velocity, temperature range). The sample is then fixed in the capillary with quartz wool plugs, and the capillary placed in the assembled support bracket (support rod and steel plates). The capillary is then treated with epoxy glue at the interface of the gas connections, providing a closed gas flow system. After hardening of the epoxy glue, the complete sample holder is transferred to the beamline stage. Sample alignment in the centre of rotation with respect to the beam is achieved using the manual goniometer (tilt/vertical alignment) and the manual linear stages (horizontal alignment). It is possible to achieve 1 μm precision during tomography scans using manual positioning, whereas small sample movements or vibrations can be corrected through post-processing alignment of the tomographic projection series. The setup is appropriate for microtomography, but higher resolutions are not currently feasible due to mechanical vibrations and the lack of feedback-controlled position correction.

Due to the small uniform heated zone of the gas blowers, the reactor as shown here is optimised primarily for gas phase chemistry, i.e. where none or a limited volume of condensable products may be formed. The gas delivery and exhaust lines were made of a polymer rather than steel and were not heated in this study. The presence of bulky heating tapes could cause significant strain or torsion on the capillary during translational or rotational movements required for tomography.

Operando Spectrotomography Data Processing

The data processing pipeline for a single *operando* spectrotomography dataset can divided into the following steps:

- Collection of projection series at 51 distinct energy points around Cu K edge (see Supplementary Table 1)
- Background removal of support rod absorption signal from each projection series
- Pre-alignment of projections from each energy point at each rotational angle (e.g. for $\theta = 37°$, align projections from 8950 to 9220 eV)
- Final alignment of projection series (e.g. for 8950 eV, align rotational angles θ = 0 to 180°), resulting in 51 aligned projection series
- Sinogram generation for each horizontal row on each of the 51 projection series
- Tomography reconstruction by simultaneous iterative reconstruction technique (SIRT)

Supplementary Table 1 – XANES scanning parameters

Start energy range [eV]	End energy range [eV]	Step size [eV]	No. steps
8950	8970	5	5
8970	9000	1	30
9000	9120	10	12
9120	9220	25	4

A single raw dataset obtained represents a 2D projection series of the monolith sample for each rotation step. Since during a limited rotation range the support rod moves between the sample and the beam and partially absorbs X-rays, this signal must be removed in order to isolate the transmission signal of the sample. Rod and background removal was therefore the first processing step, performed with the Fiji image processing package (v1.52p)[1,2]. The procedure is illustrated in

Supplementary Figure 3. The projection series at each energy point were transformed into the corresponding sinograms, where the rod is clearly visible as a horizontal line (note that sample detail was still visible behind the rod, indicating that the rod only partly attenuated the beam around Cu K edge). The rod was isolated from the sides of each sinogram and extrapolated to the same size as the original projection, this assumes that the rod has uniform thickness at the spatial resolution of the measurement (~5 μm). The extrapolated rod was then subtracted from the sinograms, and the background corrected projection series recovered.
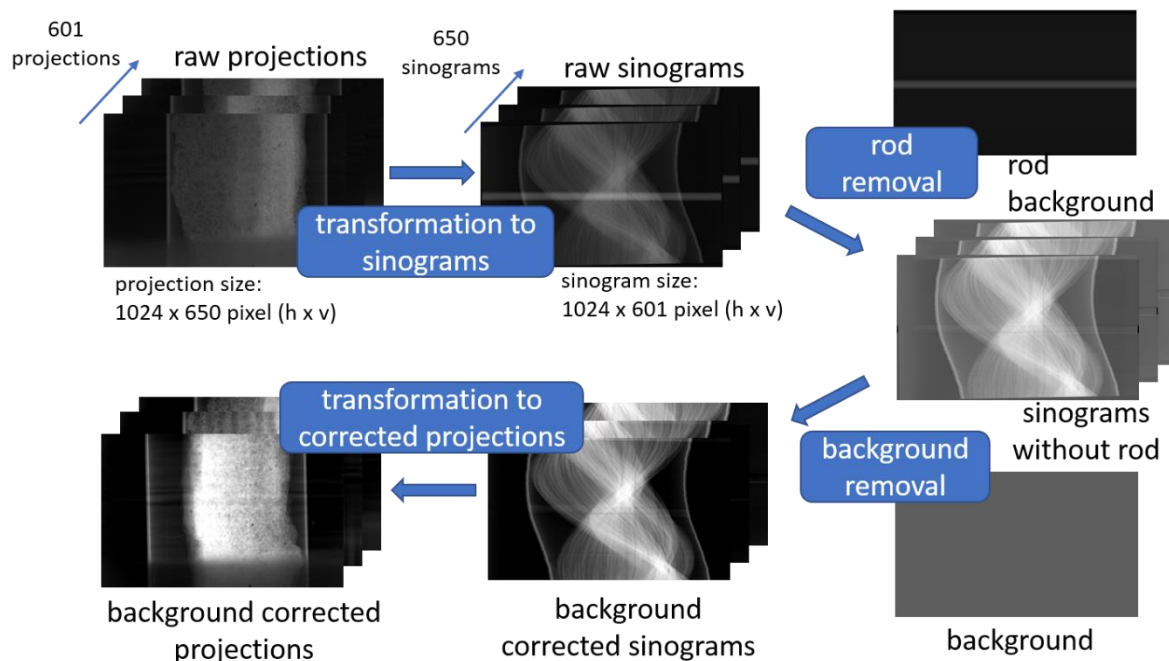
Supplementary Figure 3 – removal procedure of the support rod from the projection series, resulting background corrected projection series at each energy point.

Next, the projections from the same angle of rotation for each energy series were aligned to each other to compensate for fluctuations in the beam and movements of the sample. A second alignment was then performed of each projection series at each single energy. This resulted in 51 well-aligned projection series which could then be further reconstructed. After alignment, the projection series were reshaped into sinograms and individually reconstructed using the SIRT algorithm (iterations: 100; angle range: 180°; using CUDA; filter type: ram-lak) of the ASTRA Toolbox (v. 1.8)[3-5]. Of the 650 reconstructed slices, approximately 200 in total were discarded from the upper and lower regions which lay outside the specified field of view of the X-ray camera. This led to a total of 51 tomograms resolved in energy around the Cu K edge, each consisting of approximately 465 individual orthographic (vertical) slices of the sample with 1024*1024 pixels per slice. Assuming approximately 30% of the measured slices contained relevant sample information (70% air, capillary, or padding), a total of 146 million individual Cu K edge XANES spectra were therefore acquired at a single measurement condition. Since a total of 7 measurement conditions were performed, we estimate that over 1 billion individual XANES spectra were collected only on the monolith sample during the whole experiment.

Energy-Dispersive XAS Spectrotomography

The *operando* spectrotomography setup used (Supplementary Figure 2) was similar to that used for the full-field experiments in the current work. For energy-dispersive measurements, a larger quartz capillary of 3 mm diameter was used, and a complete channel of 1.8 wt% Cu-SSZ-13 washcoated monolith was placed inside the reactor. The support rod was also larger at 5 mm diameter, although it was a hollow tube with 1 mm wall thickness. All spectrotomography measurements were performed with a gas mixture containing 500 ppm NH_3, 500 ppm NO and 9 % O_2 in He, representing model standard SCR conditions. In total three measurements were performed, one under *ex situ* conditions at room temperature and in air, and two under SCR conditions, one at around 200 °C and one at 320 °C.

The tomographic measurements were performed at beamline ID24 of the European Synchrotron Radiation Facility (Grenoble, France)[6]. For energy-dispersive XAS a polychromatic beam was generated with a cross-section of 3 * 7 µm²

(horizontal x vertical) by focusing horizontally with a bent Si (111) polychromator, and vertically using a bent Si mirror. This resulted in a fan-shaped beam with position sensitive energy distribution. The position-sensitive detector used 1201 pixels to resolve an energy range of around 8840 to 9307 eV in a simultaneous manner. Spectrotomography scans were performed with a horizontal scanning step size of 5 μm over a total of 3.6 mm (760 steps) and for 483 projections over 180° in total. The tomographic data were measured in slices using a translate-rotate measuring scheme. The special feature of the energy dispersive measuring mode means that a complete sinogram is recorded for each detector channel. Thus, all 1201 energy points must be reconstructed individually for each measured slice. The support rod was taken into account when removing the background as described in Supplementary Figure 3. For the reconstruction of the background corrected sinograms the filtered back projection (FBP) algorithm inside the ASTRA toolbox was used[3]. The reconstructed pixel size was 20 * 20 μm². Only single slices of the catalyst were measured due to time constraints. The obtained reconstructions were binned in a 2 * 2 pixel grid to improve spectral signal to noise ratio.

Supplementary Discussion

XANES Data Processing and Linear Combination Fitting (LCF)

The reference spectra used in the LCF analysis procedure are shown in Supplementary Figure 4. The reference spectra were obtained at the SLS X10DA (Super-XAS) beamline as described previously[7,8], and summarised here. As references, the spectra of two powder Cu-SSZ-13 samples (0.5 and 1.2 wt% Cu, ca. 6 mg, sieve fraction 0.1–0.2 mm, supported by two quartz wool plugs, 7 mm bed length, 50 ml/min gas flow rate) were used. The spectra of the as received Cu-SSZ-13 (1.2 wt% Cu) measured in 10% O_2 in He at 70 °C and in 1000 ppm NO and 10% O_2 in He at 500 °C were used for representing hydrated and dehydrated Cu(II), correspondingly. As previously found[9], addition of NO to the feed is essential to prevent auto-reduction of dehydrated Cu sites at high temperatures. Two other references spectra for Cu(I) with and without directly adsorbed ammonia could not be measured separately and instead were extracted from the set of spectra obtained during temperature-programmed reduction of Cu-SSZ-13 by NH_3 using multivariate curve resolution-alternating least squares method (MCR-ALS)[10,11]. This mathematical procedure used in chemometrics allows extraction of *a priori* unknown spectra of reference compounds from a set of spectra of a mixture with changing concentrations. The technique is similar to principal component analysis but it allows setting appropriate physical constraints to the components which permits obtaining meaningful spectra. In our case constraint of non-negativity was applied to the matrix of reference spectra and constraints of unimodality (*i.e.*, having only one maximum) were applied to concentration profiles. The obtained reference spectra demonstrated all the features of Cu(I) with and without directly adsorbed ammonia as previously observed in high energy resolution fluorescence detected (HERFD)-XANES experiments and were assigned correspondingly[9]. MCR-ALS was required because the direct use of spectra available in literature as references for the LCA is not possible due to differences in spectral resolution, and the dataset obtained on the 0.5 wt% Cu-SSZ-13 was chosen since the individual features of the spectra were better resolved in this case. In the case of the 1.2 wt% Cu sample, even at high temperature the last spectrum shows the contribution of Cu^+ with directly adsorbed ammonia. The actually used reference spectra and the corresponding Cu coordination environments modelled for single Cu sites (assumption based on the fact that nuclearity of Cu species does not significantly

influence XANES[12]) are summarised in Supplementary Figure 4, adapted from previous work[7].

(a)

Mobile Cu(II) complex, CN = 5 — 70 °C — 10% O_2 in He

Mobile linear Cu(I)*NH_3 complex, CN = 2 — 275 °C — 1000ppm NH_3 in He

Cu(II) fixed to the zeolite framework, CN = 3 or 4 — 500 °C — 1000ppm NO, 10%O_2 in He

Cu(I) fixed to the zeolite framework, CN = 2 — 550 °C — 1000ppm NH_3 in He

Normalized Absorption

Energy around Cu K edge

Si, O, Cu, Al, N, H

* Cu can be localized in several different sites in the SSZ-13 framework, therefore only a schematic example is shown. Note – dehydrated Cu(II) spectra with coordination number 3 or 4 are highly similar

(b) Normalized Absorption (a.u.) — Energy (eV)
Cu(I); Cu(I)*NH_3; hydrated Cu(II); dehydrated Cu(II)

(c) Normalized Absorption (a.u.) — Energy (eV)
Cu(I); Cu(I)*NH_3; hydrated Cu(II); dehydrated Cu(II)

Supplementary Figure 4 – (a) Schematic representation of the reference spectra including coordination numbers (from EXAFS analysis[7,8]) and conditions under which the corresponding species dominate the spectrum. Adapted with permission from Kerkeni, B. et al., *J. Phys. Chem. C* **122**, 16741-16755, (2018). Copyright 2018 American Chemical Society; (b) Reference spectra of various Cu oxidation and coordination states used for fitting of the *operando* spectrotomography data, focusing on the rising edge region - normalisation -33 to -3 eV (pre-edge) and +15 to +27 eV (post edge). Short range chosen due to limited density of scanning points. (c) the same spectra normalised in a conventional way (-150 eV pre-edge, +500 eV post-edge).

Note that the figure shows only one of several possible locations of Cu relative to the 6-member ring of the SSZ-13 zeolite framework. Several locations near the 6-member ring and 8-member ring are possible (and all possible structures are depicted and analysed in detail in previous work[7]) but spectra for the same coordination number and oxidation state are too similar to be distinguished by standard XANES.

The fitted Cu K edge XANES spectra for each of the 5 regions of interest (ROIs) for the monolith sample measured from 200 to 400 °C, and for the reference tomograms obtained under NH_3 flow, and NO + O_2 flow, are shown in Supplementary Figure 5-Supplementary Figure 9. ROI designations are shown in Figure 3 in the main manuscript. Only the applied LCF range is shown (8979.5 to 8992.5 eV), together with the residuals from the fit. The Cu K XANES data from individual pixels was too noisy to perform normalisation, therefore ROI averaging from the washcoat interior to the exterior was considered to be the most relevant way of monitoring for chemical gradients. The reference tomograms acquired under NH_3 flow, and NO + O_2 flow showed relatively uniform spectra within the fitting range, therefore only the fit of ROI 1 is presented in Supplementary Figure 5. Numerical data extracted from the LCF procedure are shown in Supplementary Table 2.
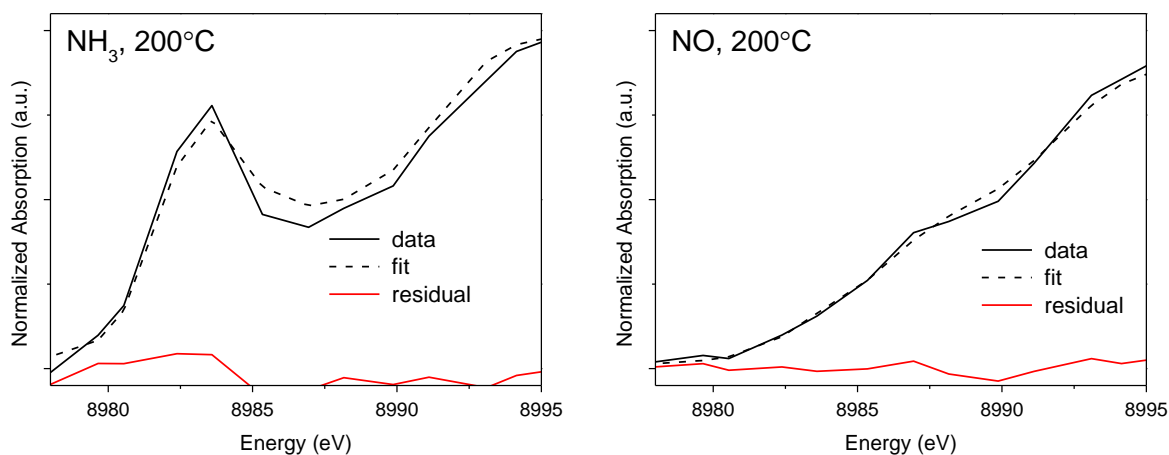
Supplementary Figure 5 – Exemplary LCF fits of the reference states (only ROI 1 is shown, other ROIs show similar spectra and fits). The fit of the spectra recorded in 1000 ppm NH_3 in He contains 74% Cu(I)*NH_3 and 26% Cu(II) (ρ = 0.7% independently on whether hydrated or dehydrated Cu(II) reference is used); the spectrum measured in 1000 ppm NO, 7.8% O_2 in He corresponds (ρ = 0.3%), to pure Cu(II) dehydrated

reference spectrum (which is, effectively, a spectrum of a powder Cu-SSZ-13 measured under analogous conditions).
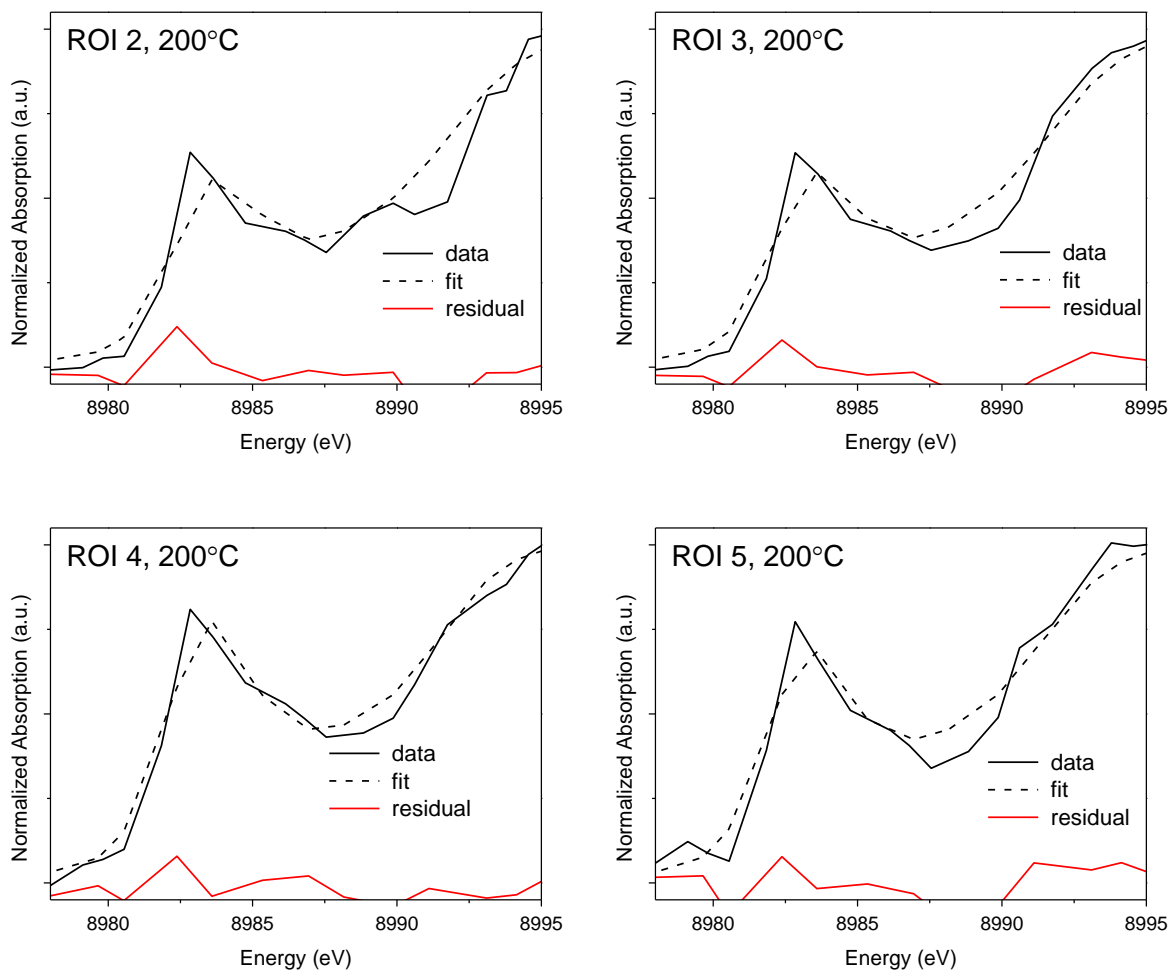
Supplementary Figure 6 – LCF fits of the *operando* XANES data acquired in ROI 2 to ROI 5 at 200 °C. Note that ROI 1 of this specific orthographic slice could not be properly normalised due to post edge distortion, therefore no fit is shown.
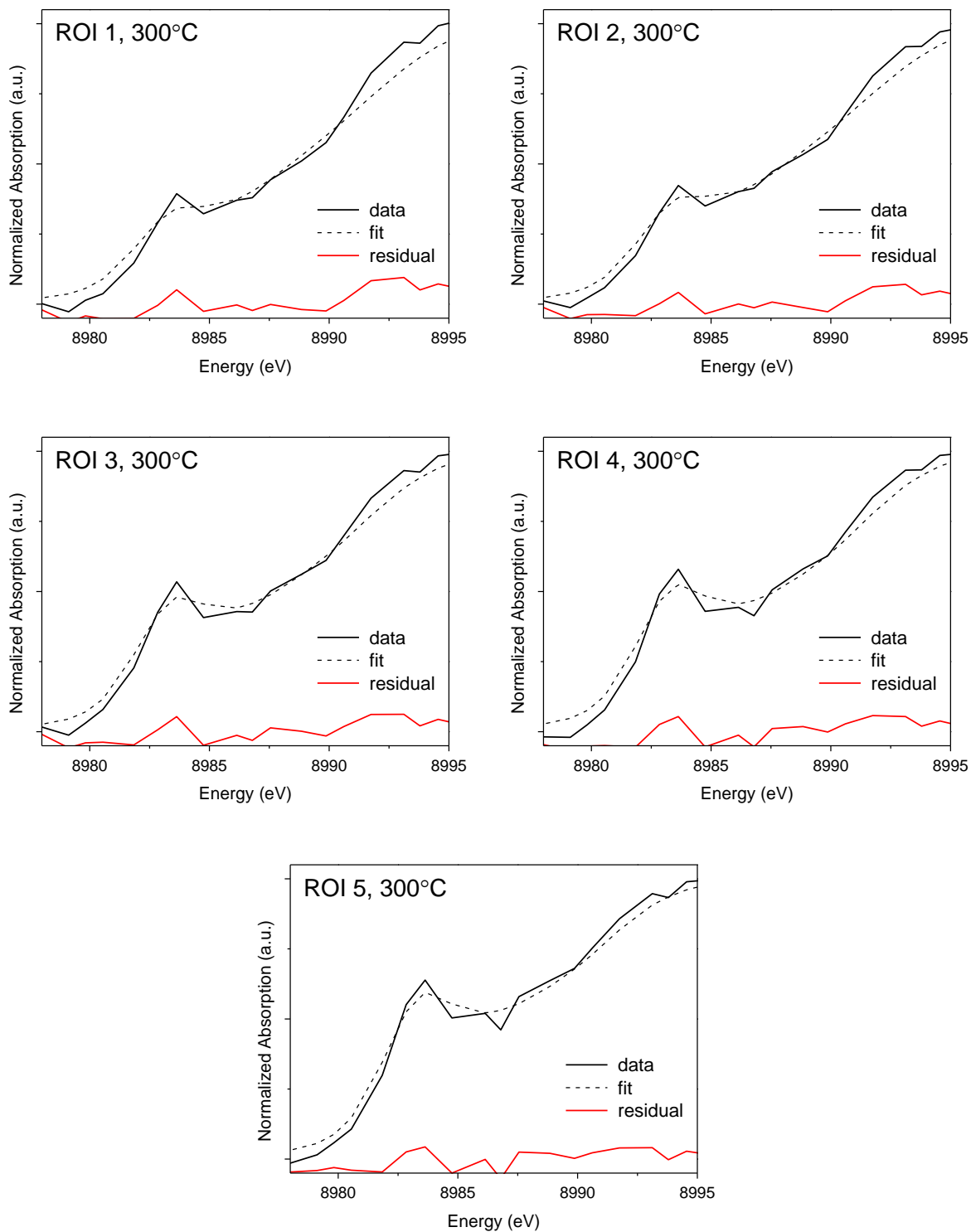
Supplementary Figure 7 – LCF fits of the *operando* XANES data acquired in ROI 1 to ROI 5 at 300 °C.
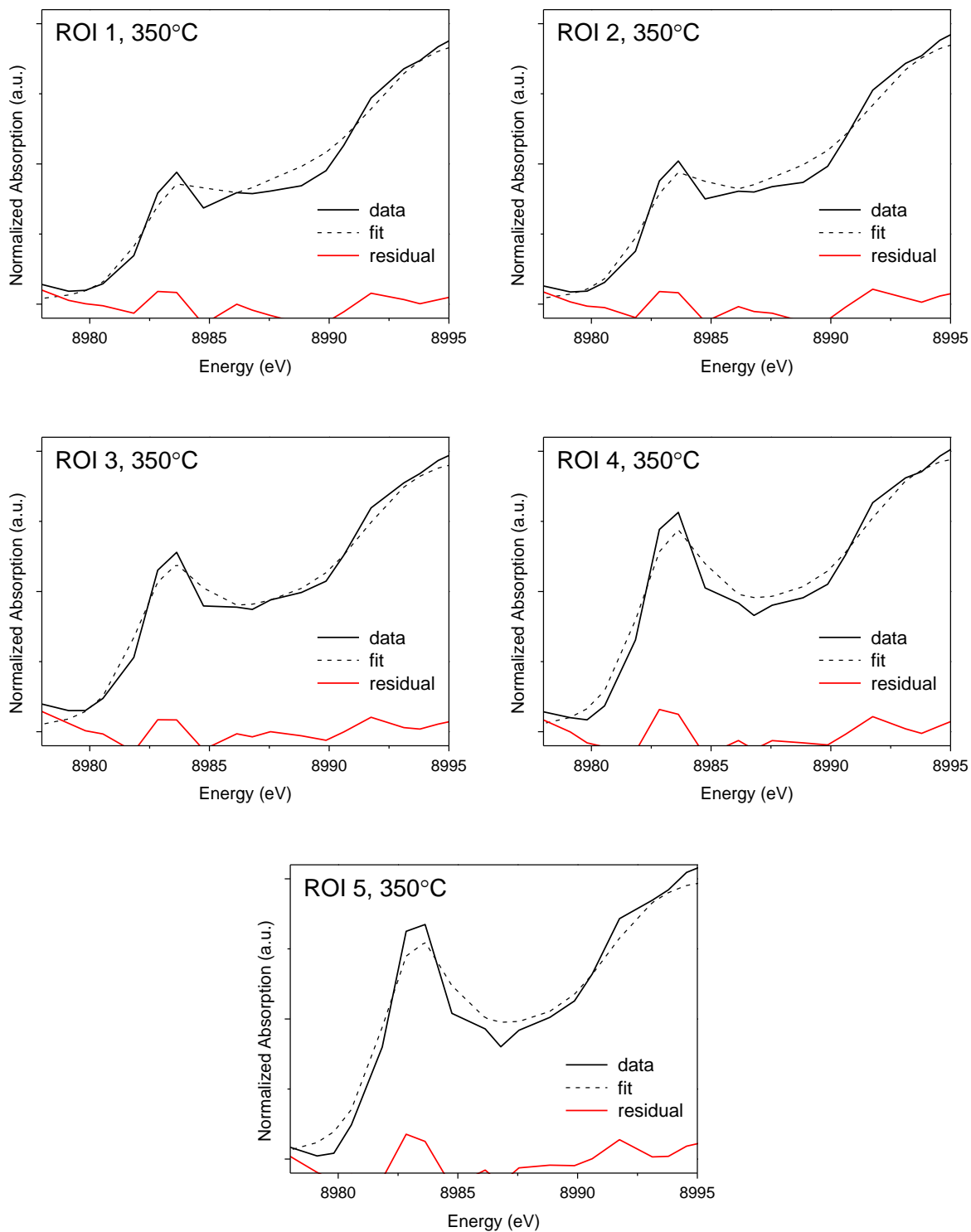
Supplementary Figure 8 – LCF fits of the *operando* XANES data acquired in ROI 1 to ROI 5 at 350 °C.
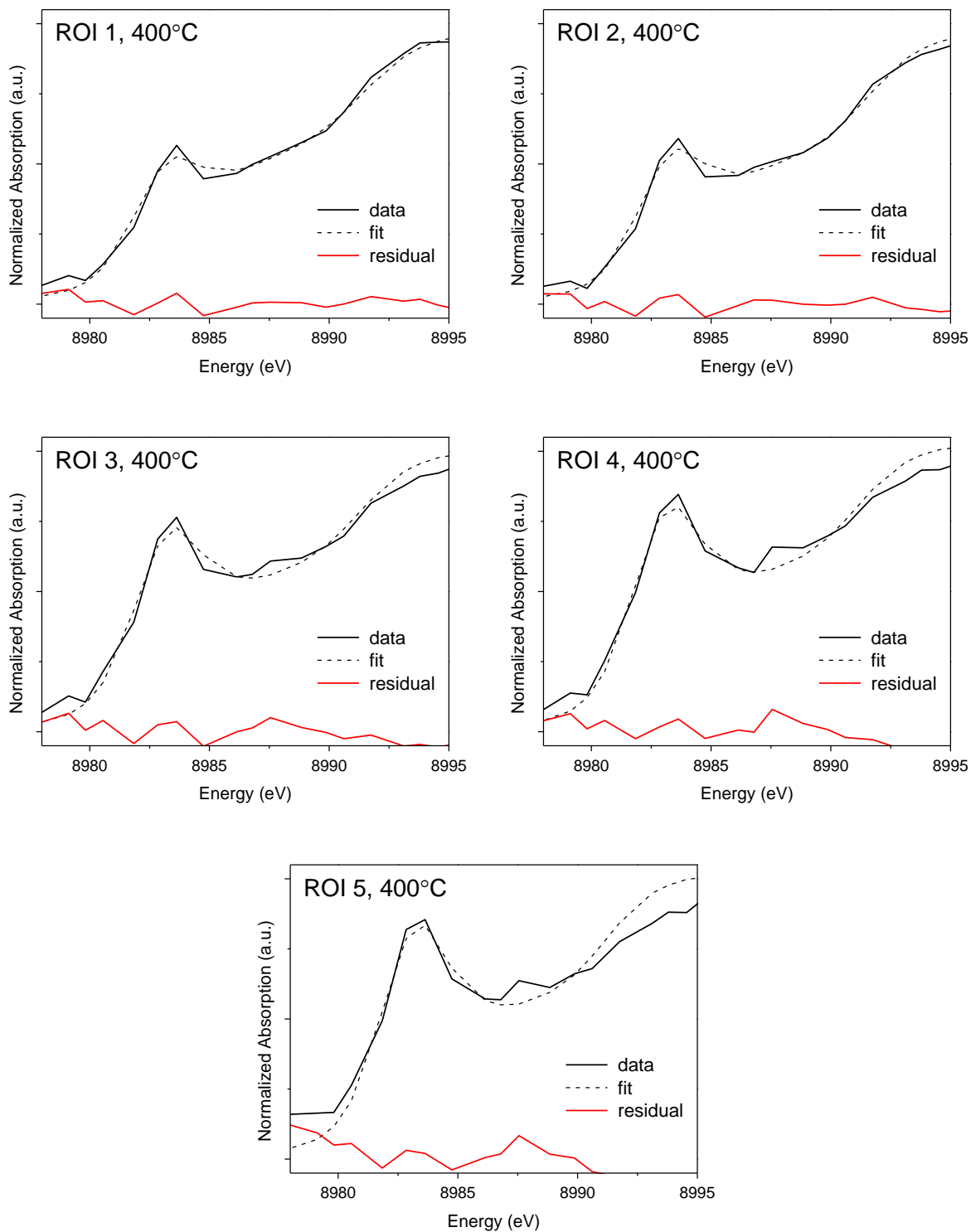
Supplementary Figure 9 – LCF fits of the *operando* XANES data acquired in ROI 1 to ROI 5 at 400 °C.

Supplementary Table 2 – Results of LCA XANES analysis in model SCR conditions

| Temp (°C) | ROI | Fraction of species (%) | | | | | E shift (eV) | ρ (%) |
		Cu(II) hydrated	Cu(II) dehydrated	Cu(I)*NH$_3$	Cu(I) - no NH$_3$	Total Cu(I)		
200	1*	0.43	0	0.57	0	0.57	0.8	4.1
	2	0.43	0	0.57	0	0.57	0.8	4.1
	3	0.41	0	0.59	0	0.59	0.6	2.2
	4	0.20	0	0.80	0	0.80	0.5	0.9
	5	0.29	0	0.71	0	0.71	0.3	1.6
300	1	0.50	0	0.13	0.37	0.50	0.1	0.7
	2	0.44	0	0.14	0.42	0.56	0.2	0.5
	3	0.33	0	0.26	0.41	0.67	0.3	0.6
	4	0.29	0	0.32	0.38	0.70	0.3	0.7
	5	0.15	0	0.32	0.53	0.85	0.3	0.4
350	1	-	0.64	0.36	0	0.36	0.6	1.0
	2	-	0.59	0.41	0	0.41	0.6	0.9
	3	-	0.44	0.56	0	0.56	0.4	0.5
	4	-	0.29	0.71	0	0.71	0.5	1.1
	5	-	0.22	0.78	0	0.78	0.3	1.2
400	1	-	0.39	0.35	0.26	0.61	0.3	0.2
	2	-	0.42	0.44	0.14	0.58	0.4	0.2
	3	-	0.09	0.55	0.36	0.91	0.2	0.3
	4	-	0	0.64	0.38	1.00	0.3	0.3
	5	-	0	0.73	0.27	1.00	0.3	0.5

*This spectrum could not be properly normalised due to post-edge distortion, however, the edge region is the same as in the ROI 2 spectrum, therefore the ROI 2 fitting results are also applied here.

Selection of Regions of Interest (ROIs) for Washcoat Analysis

The irregular-shaped ROIs chosen for gradient analysis (see Figure 3 in main manuscript) were selected in order to avoid imperfections in the washcoat material, such as small pores or cracks, which would have contributed to noise in the spectral data averaged under each ROI. To illustrate that the selection of ROIs has only a minor impact on data quality, Supplementary Figure 10 shows the XANES data extracted from symmetrical and congruent ROIs from the washcoat interior (ROI 1) to the exterior (ROI 6). Notably the presence of a chemical gradient in Cu oxidation state was still clearly observed. The choice of ROI size and shape can therefore be seen as somewhat arbitrary, given that the XANES data shown are an average of the individual pixel signals constituting the ROI.
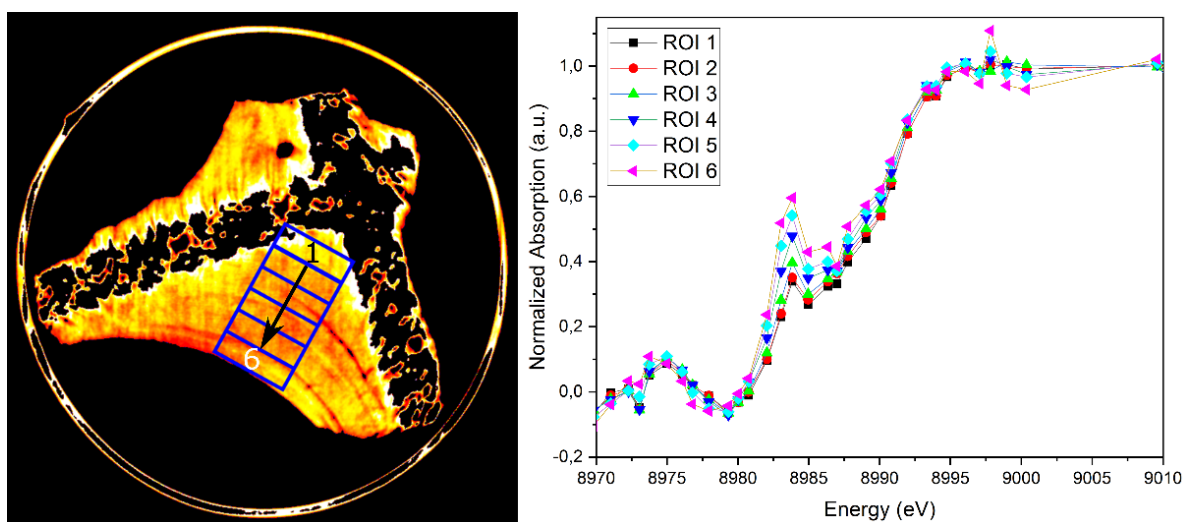
Supplementary Figure 10 – Example of the XANES data extracted from symmetrical and congruent ROIs (1 = interior of washcoat corner, 6 = exterior of washcoat corner) at 300 °C under model SCR conditions.

Comparison of Chemical Gradients by Washcoat Thickness

In order to compare the presence of gradients in copper oxidation state and coordination depending on washcoat thickness, a series of slices were selected at different axial positions of the monolith. The selected regions are indicated in Supplementary Figure 11. For accurate comparison, the same ROIs were used in all slices as for the temperature variation series in the manuscript. However, it should be noted that the washcoat does not have uniform thickness in the axial direction, thus leaving some slices with no material in the outermost region of interest (ROI 5). This was excluded in some cases from the XANES analysis.
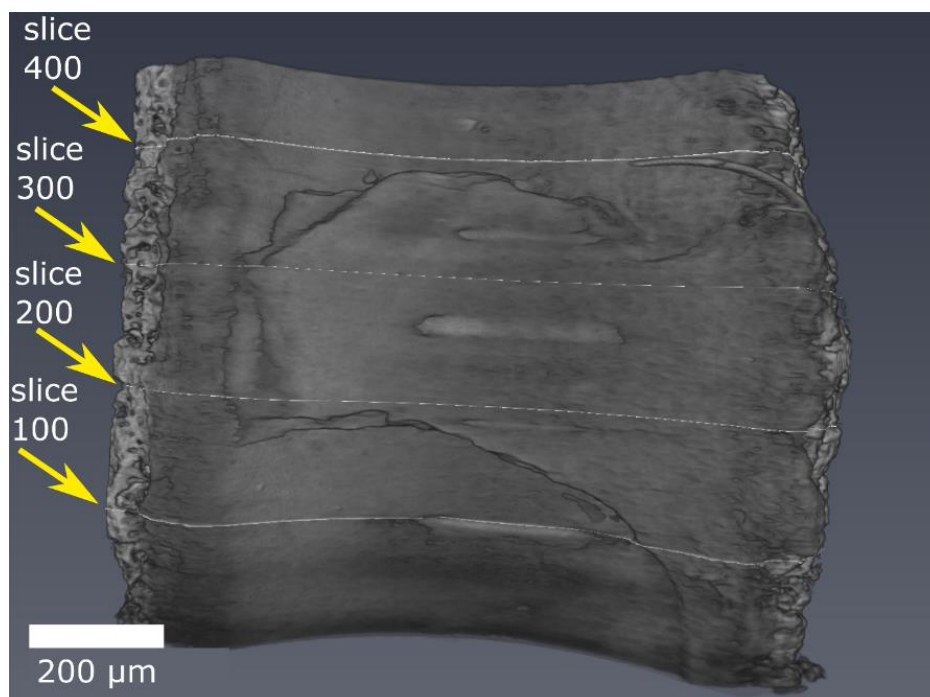
Supplementary Figure 11 – selected slices of the monolith sample (capillary not shown) for axial comparison of different washcoat thicknesses.

Full-field spectrotomography recovered a vertical field of view of around 1 mm, visualising 465 individual axial slices of the catalyst with variable washcoat thickness. Due to the nature of the full-field measurement, the slices are stacked consecutively with a thickness of around 1.6 µm per slice (effectively zero distance between slices). Operando tomography therefore offered the unique possibility to examine the chemical gradients as a function of washcoat shape from a single recorded dataset. Comparison of the XANES fitting at 350 °C revealed consistent gradients across all the examined slices, with decreased Cu(II) content and increased Cu(I) content moving from the washcoat interior at ROI 1 to the exterior at ROI 5 (Supplementary Figure 12). Note for slice 100 and 400, ROI 5 was not present due to the thin washcoat. For the thicker washcoat slices (Supplementary Figure 12 f,g), both Cu(I) with and without NH_3 were observed, while for the thinner slices (Supplementary Figure 12 e,h) Cu(I)*NH_3 was the only Cu(I) species observed. This is again consistent with mass transport limitations affecting the thicker washcoat slices. A conservative error estimation of +/- 0.15 was taken for the calculated weights of each component, reflecting the maximum uncertainty reported by the LCF subroutine of Athena 0.8.056 software[13].
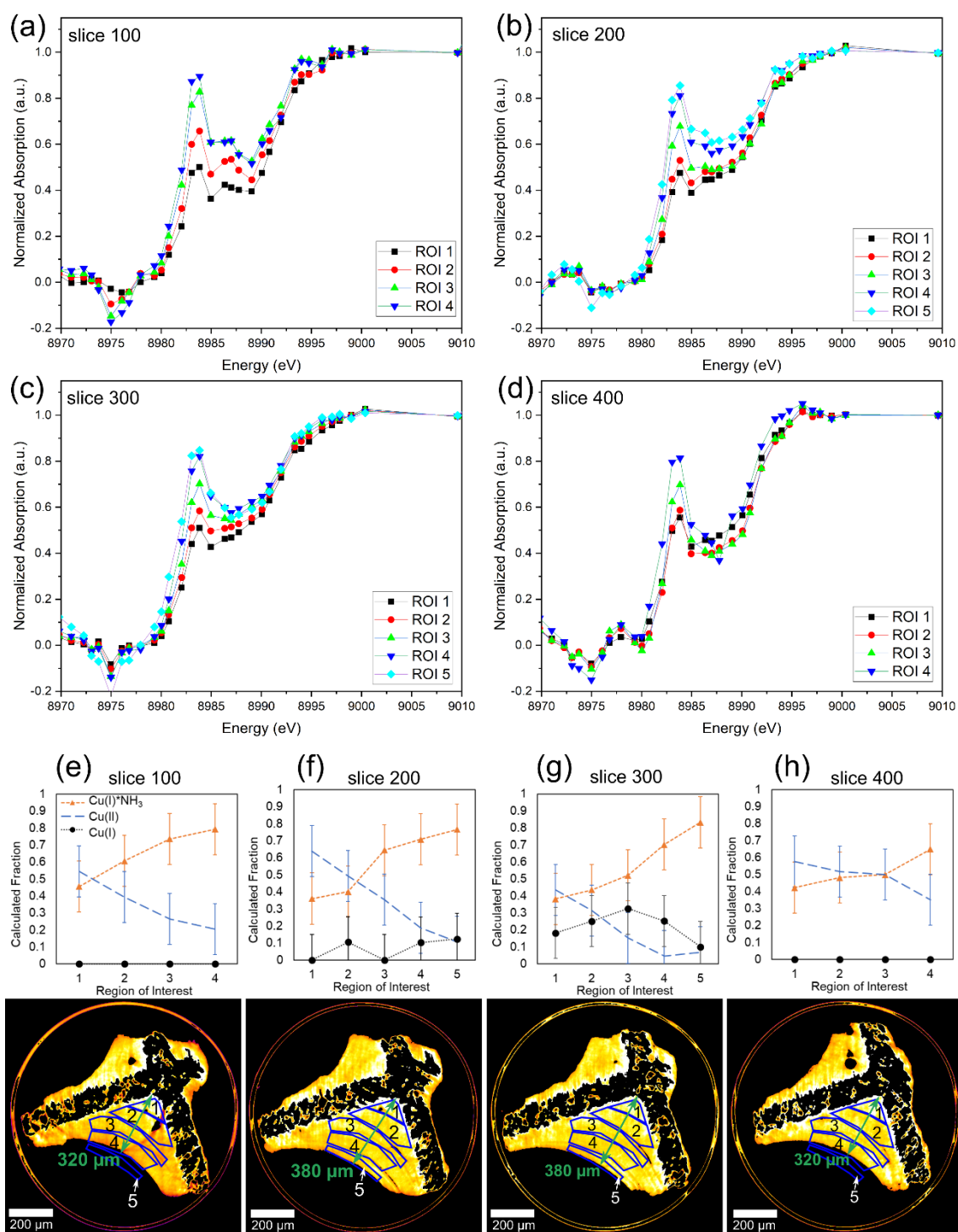
Supplementary Figure 12 (top) Normalised and fitted XANES spectra of ROIs 1 to 5 for four evenly spaced axial slices: (a) slice 100 (towards reactor inlet); (b) slice 200; (c) slice 300; (d) slice 400 (towards reactor outlet); for comparison of radial gradients with different washcoat thickness (inset – fitted slice with colour coding corresponding to the raw intensity of the XANES edge feature at 8983 eV); fitted fractions of Cu(I), Cu(I)*NH$_3$ and Cu(II) dehydrated in the XANES spectra for: (e) slice 100; (f) slice 200; (g) slice 300; (h) slice 400; showing gradients from ROIs 1 to 4. Error bars represent the maximum uncertainty reported by LCF subroutine of Athena[13].

20

Aside from the inner corner of the monolith channel, the presence of chemical gradients was also investigated on smaller washcoat fragments on the outside of the channel. These fragments, a result of the cutting process, would not be expected in an industrially-relevant catalyst, where the washcoat would be enclosed on all sides by the cordierite monolith. Nevertheless, such fragments are representative of relatively short diffusion lengths, compared to the inner corner. As shown in Supplementary Figure 13, no gradient was observed under NH_3-SCR conditions at 350 °C, while as shown in the manuscript a significant gradient in copper oxidation state was observed for the inner washcoat corner of the exact same sample slice at the same temperature. As identical conditions were applied to the entire sample, this supports the conclusion that mass transport effects were an important contributing factor to the chemical gradients observed, and furthermore proves that the observed gradients were a genuine effect and not an artefact of the imaging or tomographic reconstruction process. However, it should be noted that not only the thickness of the layer, but also the presence of the cordierite carrier material (and the thickness of the washcoat on the opposite side of the cordierite) may have an influence on the mass transport limitations by providing additional diffusion pathways. Even though those additional diffusion pathways cannot be excluded, the diffusion through the cordierite, if any, was significantly slower than through the washcoat. To prove and quantify the contribution of the diffusion through the cordierite one would need to compare the obtained data with the data predicted by macrokinetic modelling.
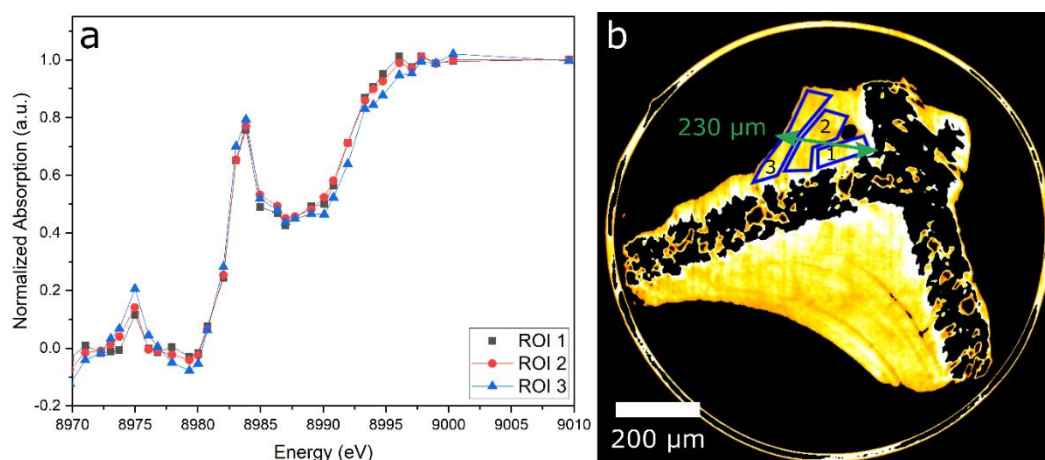
Supplementary Figure 13 – (a) Comparison of the XANES spectra of three regions of interest (ROI) in the thin outer washcoat fragment; (b) the ROIs used to extract the Cu K edge XANES spectra shown.

Operando Spectrotomography Data of Reference States

To complement the *operando* spectrotomography experiments under NH$_3$-SCR conditions and confirm the chemical gradients observed as a real feature and not an artefact from data treatment, reference data were also acquired by exposing the monolith sample to 1000 ppm NH$_3$ (in the absence of NO/O$_2$) and 1000 ppm NO / 7.8% O$_2$ (in the absence of NH$_3$) at 200 °C. For comparability, the same specific slice of the tomography data is shown as for the NH$_3$-SCR experiments in the main text. As the reference data acquired were expected to indicate uniform sample composition, they can also be used to estimate error in the measured XANES between different ROIs. Here +/- 0.15 was taken as the maximum error bar value reported by ATHENA software during the fits[13].
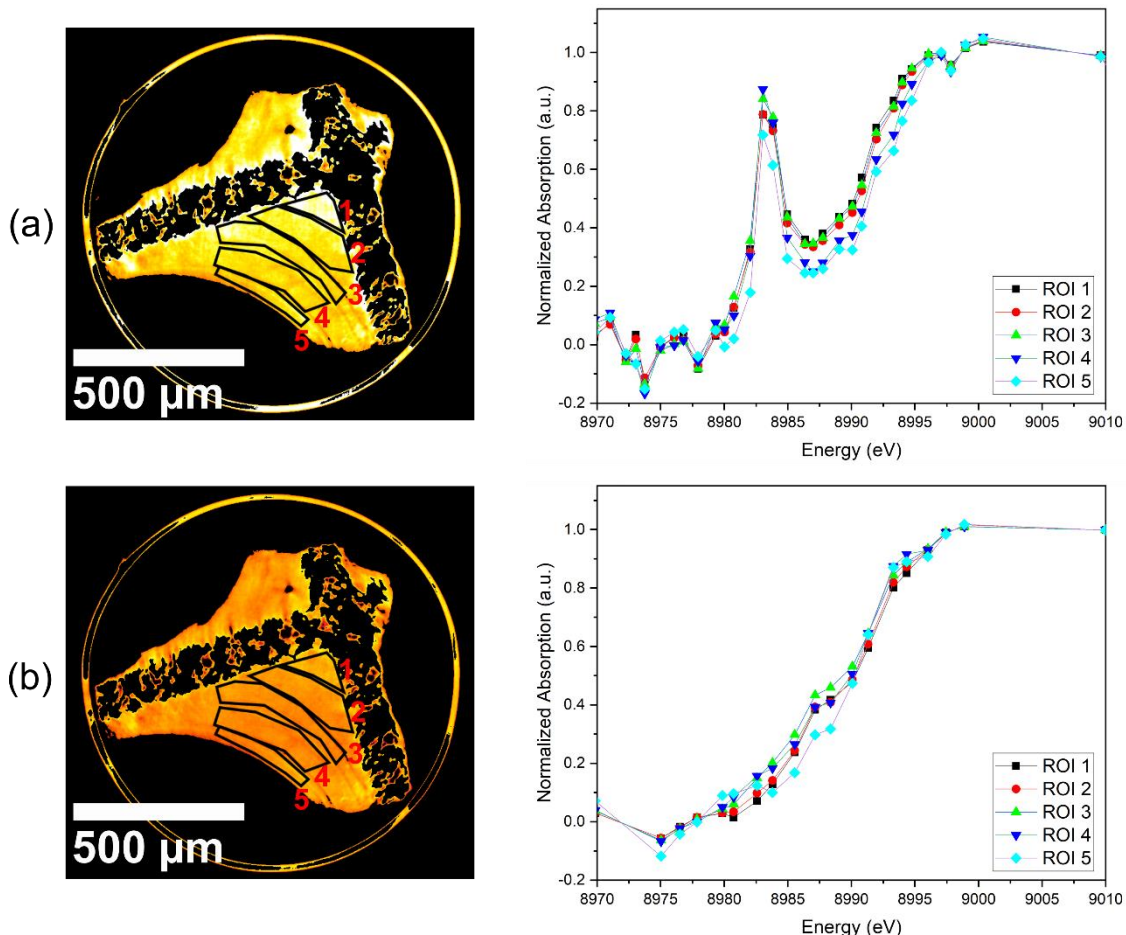
Supplementary Figure 14 – orthogonal slice of the reconstructed spectrotomography data showing ROI 1 (washcoat interior) to ROI 5 (washcoat exterior) and the corresponding average normalised XANES spectra for: (a) NH$_3$ reference (1000 ppm NH$_3$ in He) at 200 °C; (b) NO reference (1000 ppm NO, 7.8% O$_2$ in He) at 200 °C.

LCF Analysis of XANES with Internal References

Apart from the LCF analysis with reference spectra presented in Supplementary Figure 4 to Supplementary Figure 9, fitting was also performed using the internal reference conditions at 1000 ppm NH_3 (representative of fully reduced Cu(I) and with full coverage of NH_3) and 1000 ppm NO / 7.8% O_2 (representative of fully oxidised Cu(II) and with zero coverage of NH_3). The reference for Cu(I) without ammonia was used as previously. The fitting results are illustrated in Supplementary Figure 15 and Supplementary Table 3. Due to poor signal to noise of the internal references as a result of measuring only 51 energy points, and inconsistent energy shifts during fitting, it was decided to use experimentally determined conventional XAS spectra acquired previously[7] to perform the fitting presented in the manuscript.
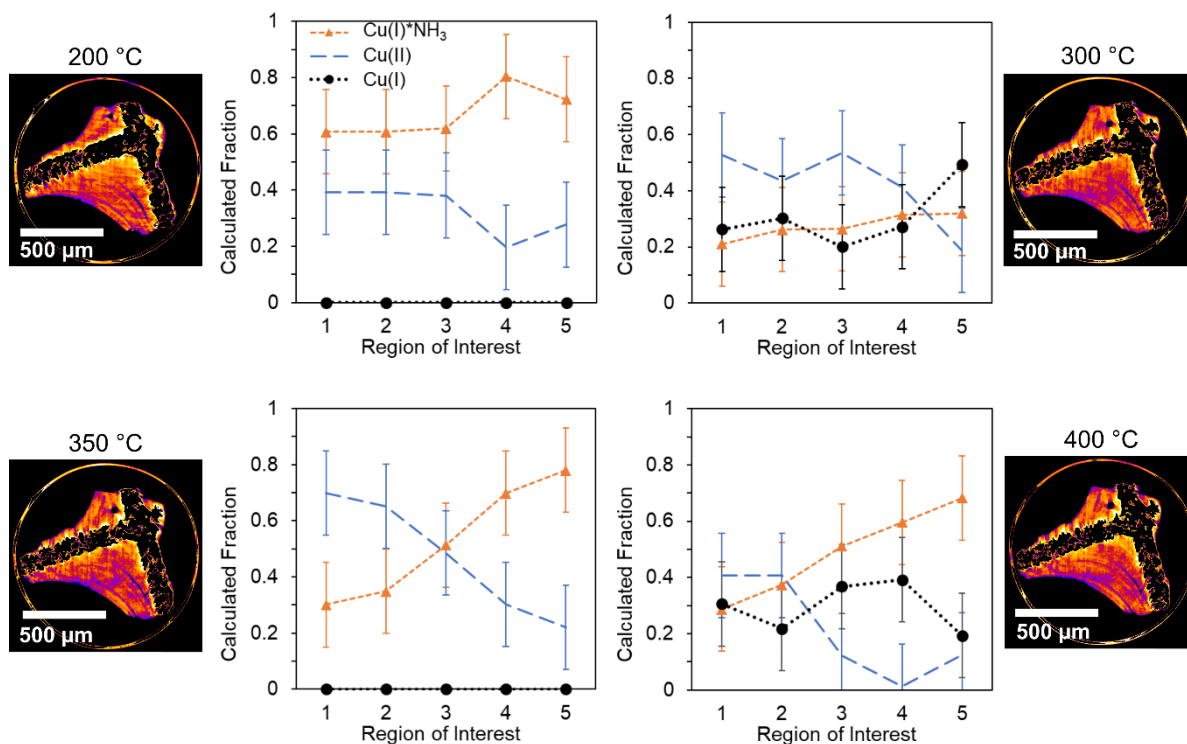
Supplementary Figure 15 – fitted fractions of Cu(I) (derived from experimental data), Cu(I)*NH_3 and Cu(II) (derived from internal references of *operando* spectrotomography data) in the XANES spectra at 200 to 400 °C. Slices are shown with colour corresponding to the raw intensity of the XANES edge feature at 8983 eV. Regions of interest are identical to Supplementary Figure 14 and the data in the manuscript. Error bars represent the maximum uncertainty reported by LCF subroutine of Athena[13].

Supplementary Table 3 – LCF fitting results using internal reference states

	200°C				
	ROI 1	ROI 2	ROI 3	ROI 4	ROI 5
Cu(II)	0.39	0.39	0.38	0.20	0.28
Cu(I)*NH₃	0.61	0.61	0.62	0.80	0.72
Cu(I)	0	0	0	0	0
R-factor	0.0197	0.0197	0.0142	0.0068	0.0248
E_shift (Cu(II))	6.69	6.69	5.67	5.38	4.47
E_shift (Cu(I)*NH₃)	0.49	0.49	0.40	0.43	0.27
E_shift (Cu(I))	n.d.	n.d.	n.d.	n.d.	n.d.

	300°C				
	ROI 1	ROI 2	ROI 3	ROI 4	ROI 5
Cu(II)	0.53	0.44	0.54	0.41	0.19
Cu(I)*NH₃	0.21	0.26	0.26	0.32	0.32
Cu(I)	0.26	0.30	0.20	0.27	0.49
R-factor	0.0089	0.0054	0.0085	0.0102	0.0054
E_shift (Cu(II))	-0.77	-0.92	-0.11	0.31	0.62
E_shift (Cu(I)*NH₃)	0.71	0.64	0.45	0.36	0.28
E_shift (Cu(I))	5.648	4.94	0.724	0.7	0.522

	350°C				
	ROI 1	ROI 2	ROI 3	ROI 4	ROI 5
Cu(II)	0.67	0.65	0.49	0.30	0.22
Cu(I)*NH₃	0.30	0.35	0.51	0.70	0.78
Cu(I)	0	0	0	0	0
R-factor	0.0090	0.0088	0.0058	0.0107	0.0125
E_shift (Cu(II))	0.86	0.72	0.45	1.24	1.36
E_shift (Cu(I)*NH₃)	0.63	0.60	0.49	0.47	0.34
E_shift (Cu(I))	n.d.	n.d.	n.d.	n.d.	n.d.

	400°C				
	ROI 1	ROI 2	ROI 3	ROI 4	ROI 5
Cu(II)	0.41	0.41	0.12	0.01	0.12
Cu(I)*NH3	0.29	0.37	0.51	0.60	0.68
Cu(I)	0.31	0.22	0.37	0.39	0.19
R-factor	0.0019	0.0026	0.0022	0.0021	0.0034
E_shift (Cu(II))	0.44	0.45	1.39	20.5	4.90
E_shift (Cu(I)*NH3)	0.37	0.44	0.46	0.39	-7.40
E_shift (Cu(I))	0.26	0.78	-0.40	-0.94	0.27

Mass Spectrometry Data during *Operando* Spectrotomography Experiments

The mass spectrometer present downstream of the reactor was operated continuously for over 100 hours, therefore the signals of all relevant species recorded specifically during *operando* spectrotomography scans under NH_3-SCR reaction conditions from 200 to 400 °C are shown in Supplementary Figure 16. To account for signal drift, all gas traces were normalised to the signal of He as an inert species, which was kept constant during the entire study. The complete absence of Ar (m/z = 40) and relatively low trace of N_2 (m/z = 28, 14) confirmed that no leaks were present and the appropriate standard SCR conditions were maintained at all times. Low conversion of NO and a non-linear trace of m/z 28 was observed at 200 °C, however due to the presence of chemical gradients observed already at this temperature and the absence of any gradients in the room temperature or reference scans, it is suggested that the reaction was occurring at this temperature, in accordance with previous experiments[8]. Notably, the unstable signal affected only m/z = 28, but not m/z = 14, and therefore it is difficult to attribute this non-linear effect to the behaviour of N_2, since the trace at m/z = 14 was stable at all times. The cause of the non-linear signal for m/z = 28 at 200 °C is therefore unknown, although the effect is small in magnitude and affected only the first *operando* spectrotomography experiment. In addition, the mass spectrometer was installed and put into operation on the same day as the experiments started, ideally such instruments should be pumped down and stabilised for at least a day before use. However, the nature of limited access time to the synchrotron facility did not allow for this.
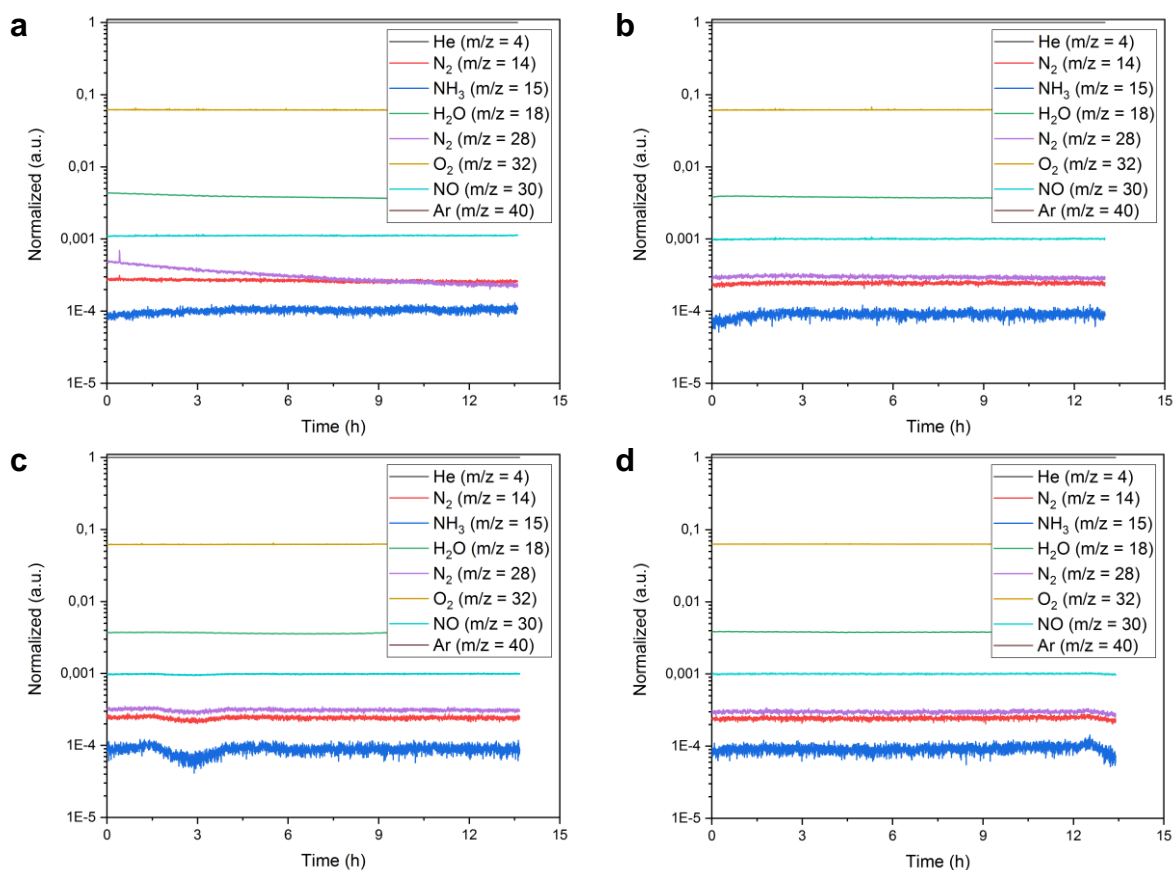
Supplementary Figure 16 – mass spectrometer data recorded at the reactor outlet during tomography scans at four different model SCR conditions (note log scale for normalised ion current).

Regarding room temperature measurements for NO (not shown) which were used as a baseline to estimate conversion, a proportional decrease in NO signal (m/z = 30) and increase in N_2 signals (m/z = 28, 14) above 200 °C (note logarithmic scale) indicates the NH_3-SCR proceeding as intended. The failure to reach 100% conversion with a 1.8 wt% Cu-SSZ-13 catalyst is a combination of high gas bypass through the reactor without significant interaction with the catalyst, and mass transport limitations, restricting the proportion of the catalyst bed which was operating at full efficiency. Nevertheless, the acquisition of quantitative catalytic performance data proves that the experiments were performed under *operando* conditions. At the same time, low conversion of 10% at 300 to 400 °C ensures little or negligible axial concentration gradients in the tested catalyst volume. If high conversions were obtained, this could lead to gradients in axial direction as a result of changing reactant concentration along the bed. This may not allow conclusive observation of gradients as the result of internal mass transport limitations, rather than simply the change in local gas environment.

Results of Energy-Dispersive XAS Spectrotomography at Cu K Edge

An overview of the measured sample and a typical spectrum acquired over a region of interest encompassing most of the washcoat is shown in Supplementary Figure 17. The energy-dispersive spectrotomography measurements resulted in reasonably high quality XANES spectra after binning and averaging. After normalisation of the XANES spectra of the washcoat of each measured condition (ambient temperature in air, NH_3-SCR at 200 °C and 320 °C), it was noted that only Cu(II) was visible in spectra (Supplementary Figure 18). While only a small section of data is shown here, no visible gradients could be observed under any of the measured conditions, unlike the full-field spectrotomography experiments discussed in the manuscript. It was assumed that the high intensity polychromatic beam can stimulate spontaneous oxidation of the sample, and desorption of NH_3 from the catalyst surface. In the specific case of NH_3-SCR on Cu-SSZ-13, the presence of adsorbates plays a critical role in the catalytic mechanism, therefore the lower local X-ray dose associated to full-field tomography was found to be optimal, compared to the intense polychromatic beam from energy-dispersive XAS. In comparison, energy-dispersive XAS experiments at ID24 had a flux of approx. $1*10^{13}$ photons/s focused on a spot size of around 3 * 7 µm² and an energy bandwidth of approx. 1000 eV (polychromatic beam). Full-field measurements at microXAS had a flux of approx. $1*10^{12}$ photons/s dispersed over an area of approx. 1500 * 1000 µm² and an energy bandwidth of approx. 0.4 eV (monochromatic beam). The instantaneous dose to the sample during full-field measurements was therefore much lower than for energy-dispersive XAS.

It should be noted that energy-dispersive XAS is a valid approach of interest in future studies. This is primarily due to the extremely efficient simultaneous acquisition of energy-resolved data in a wider spectral range than is feasible with full-field XANES spectrotomography, and much more rapidly than with conventional XAS. On the other hand, energy-dispersive XAS is a scanning microprobe technique, meaning that while all energy points can be acquired at a single spatial position simultaneously, the spatial scanning requirements (translation followed by rotation) are much more extensive than for full-field imaging, where all spatial data points are acquired simultaneously. For such experiments to be successful in future, it is essential to minimise either the time constraint or the energy constraint where spectrotomographic imaging is required. This

is independent of whether an *operando* study is performed, which only requires the simultaneous application of relevant reaction conditions and acquisition of quantitative activity data during the spectrotomography scan.
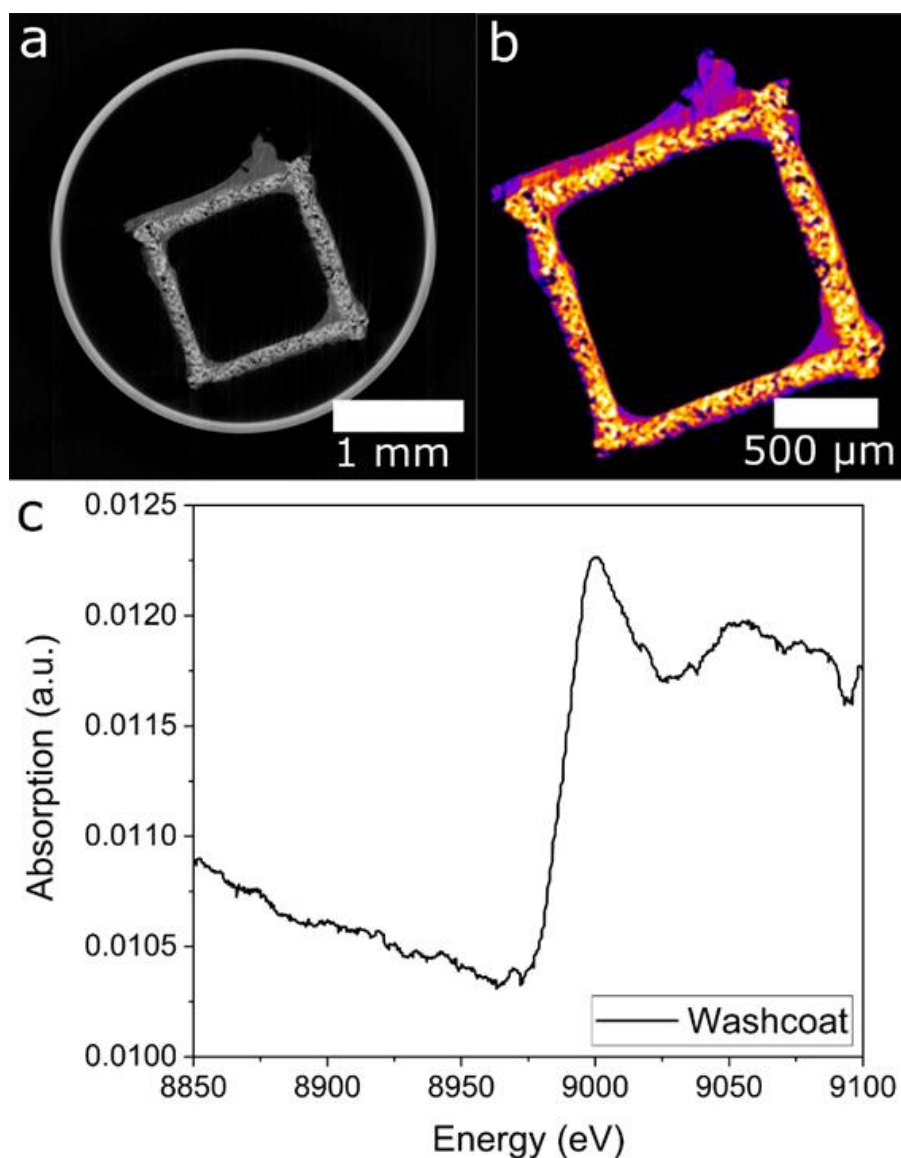
Supplementary Figure 17 – (a) reconstructed energy-dispersive tomography slice showing the complete monolith channel inside the quartz capillary; (b) cropped reconstruction with colour coding depicting the intensity of absorption at 8983 eV; (c) example XANES spectra at Cu K edge, averaged over 90% of the washcoat material in the lower right corner.
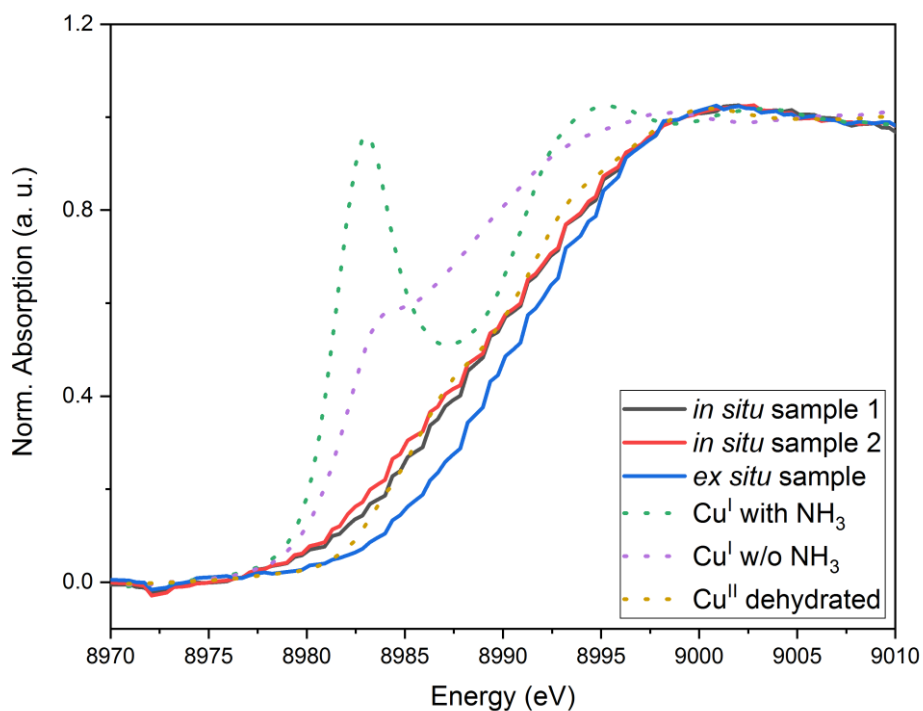
Supplementary Figure 18 – energy-dispersive XANES spectra of the washcoat material under ex situ conditions, NH$_3$-SCR conditions at 200 °C (*in situ* sample 1) and 320 °C (*in situ* sample 2). The reference spectra presented and normalisation parameters are the same as those used for the full-field spectrotomography data shown in the manuscript.

Supplementary Note 1

Development of *Operando* Spectrotomography

Although the concept of *operando* spectrotomography has excellent potential for characterising catalysts at work, there are still significant challenges involved: (i) development of sample environments, as discussed in Supplementary Methods; (ii) data acquisition and access to synchrotron radiation; (iii) data handling and processing on of millions/billions of individual spectra. In terms of data acquisition, *operando* spectrotomography demands a considerable time investment since it is necessary to scan both in energy and three spatial dimensions. Conventional tomography at fixed energy always requires data acquisition in three spatial dimensions (if more than one slice is required) and depending on the resolution required can be time consuming. However, in the present work this would not have allowed identification of individual metal oxidation states or coordination environments if performed at a single energy point, rather the results would simply be absorption contrast tomography. The need to obtain energy-resolved tomography data for spectroscopic analysis around Cu K edge therefore introduces an additional level of complexity and a large time investment. In the current work an estimated 1 billion meaningful spectra were recorded (considering only the catalyst washcoat) with 51 energy points, much less than the approximately 1000 points recorded in conventional EXAFS. As a very wide approximation, to acquire the same data with conventional XAS (general assumption of 1 to 5 seconds per scan) would take up to 150 years of continuous scanning at the synchrotron. Even with a large error in approximation, this is clearly unfeasible by around 4 orders of magnitude. In the course of this work we identified two distinct approaches to relax the time requirement:

(i) energy-dispersive XAS, where a polychromatic beam is used to measure the entire relevant XANES range of each sampling point in a single shot, relaxing the need to scan energy[14];

(ii) full-field tomography, where a broad beam is used to measure 2D projections of the entire sample at each energy, relaxing the need to scan sample positions[15,16].

While full-field tomography is presented in the manuscript, preliminary investigations with energy-dispersive XAS constituted a valuable step towards commissioning and optimising the *operando* spectrotomography setup, as discussed below.

Regarding the decision to scan a washcoat corner, rather than a full channel, this was a decision made in view of balancing the desired spatial resolution (here a target of around 5 µm), with the time investment for scanning larger samples, and the limited beamtime available. The washcoat corner could be used in a 1 mm diameter capillary, whereas to scan an entire channel (edge length 1.27 mm) would require at least a 2 or 3 mm capillary, thereby greatly increasing scan time required to achieve the desired spatial resolution. In addition, the limited horizontal field of view of the X-ray camera must also be considered. Furthermore, the washcoat corner presented a relatively similar pathlength of the X-ray through the absorber material (in this case Cu-SSZ-13), whereas to measure only a wall section, or a single channel can present additional difficulties in calculating a reasonable XANES signal due to the unusual sample geometry.

Regarding spectral quality, the time investment required for *operando* spectrotomography currently requires a compromise either in desired spatial resolution, desired field of view (sample size), or the XANES spectral quality – which is directly related to the number of individual energy points at which tomography is recorded. It should be noted that current work deals with the first practical implementation of *operando* spectrotomography, leaving considerable room for optimisation of the data acquisition process. For example, the use of an X-ray camera with faster readout time (~200 ms in this work) or greater sensitivity could allow an improvement in scan speed by a factor of approximately 3-4. In addition, optimisation of scan parameters, motor movements and beamline control systems could provide modest improvements. Perhaps more notably, the current development of next generation diffraction-limited synchrotron storage rings will offer hard X-rays with several orders of magnitude higher brilliance, which will in turn permit more rapid data acquisition. Independent of synchrotron-based optimisation, the *operando* spectrotomography setup as presented here is fully functioning at present and is therefore capable of taking advantage of any parallel improvements in beamline performance as these become available.

Supplementary References

1   Schindelin, J. et al. Fiji: an open-source platform for biological-image analysis. *Nat. Methods* **9**, 676-682 (2012).

2   Schneider, C. A., Rasband, W. S. & Eliceiri, K. W. NIH Image to ImageJ: 25 years of image analysis. *Nat. Methods* **9**, 671-675 (2012).

3   van Aarle, W. et al. Fast and flexible X-ray tomography using the ASTRA toolbox. *Opt. Express* **24**, 25129-25147 (2016).

4   van Aarle, W. et al. The ASTRA Toolbox: A platform for advanced algorithm development in electron tomography. *Ultramicroscopy* **157**, 35-47 (2015).

5   Palenstijn, W. J., Batenburg, K. J. & Sijbers, J. Performance improvements for iterative electron tomography reconstruction using graphics processing units (GPUs). *J. Struct. Biol.* **176**, 250-253 (2011).

6   Pascarelli, S., Mathon, O., Munoz, M., Mairs, T. & Susini, J. Energy-dispersive absorption spectroscopy for hard-X-ray micro-XAS applications. *J. Synchrotron Radiat.* **13**, 351-358 (2006).

7   Kerkeni, B. et al. Copper Coordination to Water and Ammonia in CuII-Exchanged SSZ-13: Atomistic Insights from DFT Calculations and in Situ XAS Experiments. *J. Phys. Chem. C* **122**, 16741-16755 (2018).

8   Fahami, A. R. et al. The dynamic nature of Cu sites in Cu-SSZ-13 and the origin of the seagull NOx conversion profile during NH3-SCR. *React. Chem. Eng.* **4**, 1000-1018 (2019).

9   Günter, T. *et al.* Structural snapshots of the SCR reaction mechanism on Cu-SSZ-13. *Chem. Commun.* **51**, 9227-9230 (2015).

10   de Jaun, A., Jaumot, J. & Tauler, R. Multivariate Curve Resolution (MCR). Solving the mixture analysis problem. *Anal. Methods* **6**, 4964-4976 (2014).

11   Jaumot, J., de Jaun, A. & Tauler, R. MCR-ALS GUI 2.0: New features and applications. *Chemometr. Intell. Lab.* **140**, 1-12 (2015).

12   Pankin, I.A., Martini, A., Lomachenko, K.A., Soldatov, A.V., Bordiga, S. & Borfecchia, A. Identifying Cu-oxo species in Cu-zeolites by XAS: A theoretical survey by DFT-assisted XANES simulation and EXAFS wavelet transform. *Catal. Today.* **345**, 125-135 (2020).

13   Ravel, B. & Newville, M. ATHENA, ARTEMIS, HEPHAESTUS: data analysis for X-ray absorption spectroscopy using IFEFFIT. *J. Synchrotron Radiat.* **12**, 537-541 (2005).

14   Ihli, J. et al. Localization and Speciation of Iron Impurities within a Fluid Catalytic Cracking Catalyst. *Angew. Chem. Int. Ed.* **56**, 14031-14035 (2017).

15	Meirer, F. et al. Mapping Metals Incorporation of a Whole Single Catalyst Particle Using Element Specific X-ray Nanotomography. *J. Am. Chem. Soc.* **137**, 102-105 (2015).

16	Meirer, F. et al. Three-dimensional imaging of chemical phase transformations at the nanoscale with full-field transmission X-ray microscopy. *J. Synchrotron Radiat.* **18**, 773-781 (2011).